


Hybrid $k \cdot p$ tight-binding model for subbands and infrared intersubband optics in few-layer films of transition-metal dichalcogenides: MoS_2 , MoSe_2 , WS_2 , and WSe_2

David A. Ruiz-Tijerina, Mark Danovich, Celal Yelgel, Viktor Zólyomi, and Vladimir I. Fal'ko
National Graphene Institute, University of Manchester, Booth St E, Manchester M13 9PL, United Kingdom

 (Received 25 March 2018; revised manuscript received 9 June 2018; published 6 July 2018)

We present a density functional theory parametrized hybrid $k \cdot p$ tight-binding model for electronic properties of atomically thin films of transition-metal dichalcogenides, $2\text{H-}MX_2$ ($M = \text{Mo, W}$; $X = \text{S, Se}$). We use this model to analyze intersubband transitions in p - and n -doped $2\text{H-}MX_2$ films and predict the line shapes of the intersubband excitations, determined by the subband-dependent two-dimensional electron and hole masses, as well as excitation lifetimes due to emission and absorption of optical phonons. We find that the intersubband spectra of atomically thin films of the $2\text{H-}MX_2$ family with thicknesses of $N = 2$ to 7 layers densely cover the infrared spectral range of wavelengths between 2 and $30 \mu\text{m}$. The detailed analysis presented in this paper shows that for thin n -doped films, the electronic dispersion and spin-valley degeneracy of the lowest-energy subbands oscillate between odd and even number of layers, which may also offer interesting opportunities for quantum Hall effect studies in these systems.

DOI: [10.1103/PhysRevB.98.035411](https://doi.org/10.1103/PhysRevB.98.035411)

I. INTRODUCTION

The $2\text{H-}MX_2$ transition-metal dichalcogenide compounds ($M = \text{Mo, W}$; $X = \text{S, Se}$) are layered materials, where chalcogens and metal atoms form covalent bonds within two-dimensional (2D) layers with hexagonal lattice structure, and neighboring layers couple weakly through electrical quadrupole and van der Waals interactions. This feature of chemical bonding makes atomically thin films of MX_2 sufficiently stable for extensive experimental studies aimed at their implementation in various optoelectronic devices [1–3]. In those recent studies, the closest attention has been paid to the interband optical properties of the monolayer transition-metal dichalcogenide (TMD) crystals [4–7], due to their direct band gap [8], valley-spin coupling [9–11], and long spin and valley memory of photoexcited carriers [12], spiced up by the Berry curvature effects for electrons and excitons in these two-dimensional semiconductors [13,14]. This is because in monolayer MoS_2 , MoSe_2 , WS_2 , and WSe_2 the valence and conduction band edges both appear at the Brillouin zone (BZ) corners K and K' , where the electronic Bloch states carry intrinsic angular momentum.

Thicker crystals of $2\text{H-}MX_2$ quickly lose the direct band-gap property upon increasing the film thickness to two or three layers [15–22]. Density functional theory (DFT) of few-layer transition-metal dichalcogenides predicts [18,20] that, for holes, the band edge relocates to the Γ point, whereas for electrons it appears at six points situated somewhere near the Q points at the middle of each ΓK segment (see inset in Fig. 1). This has been demonstrated by studies of Shubnikov–de Haas oscillations in n -doped MoS_2 [23]. While the indirect character of few-layer TMD band structures suppresses their interband photo response, the multiplicity of subbands $n|N$ ($1 \leq n \leq N$) at the conduction and valence band edges of the N -layer crystal open a new avenue for optical studies of atomically thin TMD films.

Here, we analyze theoretically intersubband transitions in few-layer MoS_2 , MoSe_2 , WS_2 and WSe_2 , and show that the absorption/emission spectra of the primary transitions in p - and n -doped crystals (Fig. 1) densely cover the infrared (IR) spectrum down to the far-infrared range (FIR) of photon energies. The analysis of subband properties of few-layer $2\text{H-}MX_2$ presented in this paper is based on the hybrid $k \cdot p$ theory tight-binding model (HkpTB) approach, recently applied to the description of multilayer films of post-transitional-metal chalcogenides (such as InSe and GaSe) [24,25]. This approach consists of minimal $k \cdot p$ theory Hamiltonians for $2\text{H-}MX_2$ monolayers [26,27], supplemented by a $k \cdot p$ expansion of the interlayer hopping near the relevant point (here, Γ or Q) in the BZ, with all parameters fitted to DFT calculated few-layer dispersions, and k_z dispersions in bulk crystals.

First, in Sec. II we describe the lattice structure and discuss symmetries of few-layer 2D crystals of $2\text{H-}MX_2$, especially the difference between films with odd and even numbers of layers and the corresponding degeneracies in their band structures. The DFT parametrized HkpTB models for few-layer TMDs are formulated in Secs. III and IV for the valence band edge (holes) near the Γ point and for the conduction band (electrons) near the Q points, respectively.

In the case of n -doped films, our models predict a multivalley subband structure with two valley triads connected by time-reversal symmetry, each consisting of three valleys related by C_3 rotations. We find that the lowest-energy subbands alternate between spin-split and spin-degenerate with number of layers N , consequence of the σ_h mirror and full inversion symmetries of films with odd and even N , respectively. These band structure features open a variety of new possibilities for studies of quantum Hall physics in multilayer TMD films.

We calculate subband energies, dispersions, and wave functions of electron/hole subbands in N -layer crystals of all four $2\text{H-}MX_2$ compounds, and optical oscillator strengths for radiative intersubband transitions. In particular, we take into

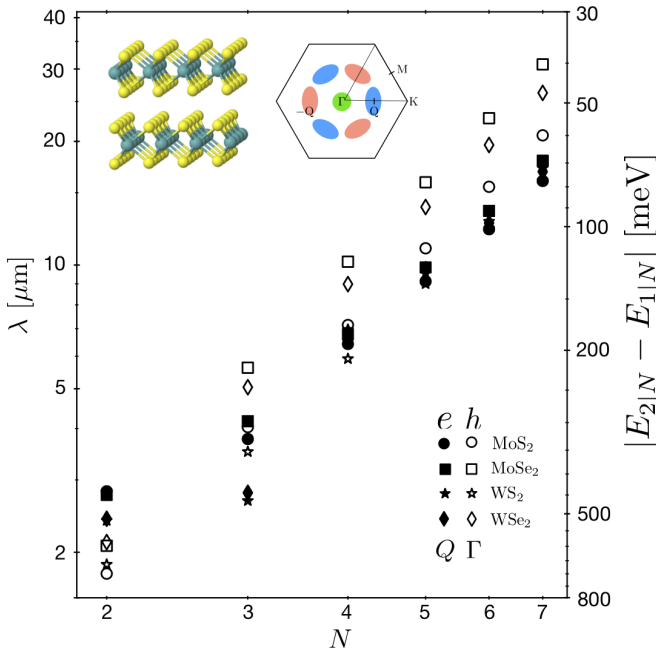


FIG. 1. Energy spacings between the first two conduction (filled symbols) and valence (empty symbols) subbands $1|N$ and $2|N$ as a function of number of layers N of the four TMDs, corresponding to n and p doping, respectively, for $2 \leq N \leq 7$. Both axes are in log scale, showing the approximate quadratic dependence of the spacings on the number of layers. The left vertical axis shows the wavelength λ in μm , corresponding to the energy spacings shown along the right vertical axis in meV. The inset shows the building block of 2H- MX_2 bulk crystals, composed of two monolayers with metal atoms in the middle and chalcogens in the outer sublayers of each monolayer, and the Brillouin zone with the Γ point and Q valleys highlighted, corresponding to the conduction and valence band edges.

account n - and p -type doping using a self-consistent analysis of charge and potential distributions across the film. Then, we analyze the inelastic broadening due to optical phonon emission, and the resulting spectral line shapes of IR/FIR absorption by p - and n -doped 2H- MX_2 films. We find that the intersubband relaxation rates, determined by electron-phonon interactions, are much slower (one to two orders of magnitude) than the intrasubband relaxation in the same materials [28,29], and also these are an order of magnitude slower than intersubband relaxation of electrons and holes in III-V semiconductor quantum wells [30]. Also, in Sec. III B we show that the difference between the two-dimensional masses $m_{1|N}$ and $m_{2|N}$ of electrons and holes in consecutive subbands leads to an additional temperature-dependent broadening of the intersubband transitions $\sigma \sim |1 - \frac{m_{1|N}}{m_{2|N}}| \max\{k_B T, \epsilon_F\}$, which appears to be the dominant intrinsic broadening effect for the IR/FIR absorption by 2H- MX_2 films at room temperature.

II. MULTILAYERS OF HEXAGONAL TRANSITION-METAL DICHALCOGENIDES: OVERVIEW

The lattice structure of monolayer TMDs MX_2 ($M = \text{Mo, W}$; $X = \text{S, Se}$) contains two hexagonal sublattices of metal and chalcogen atoms in its unit cell, as shown in Fig. 2(b). The chalcogens form two sublayers, one above and one below the

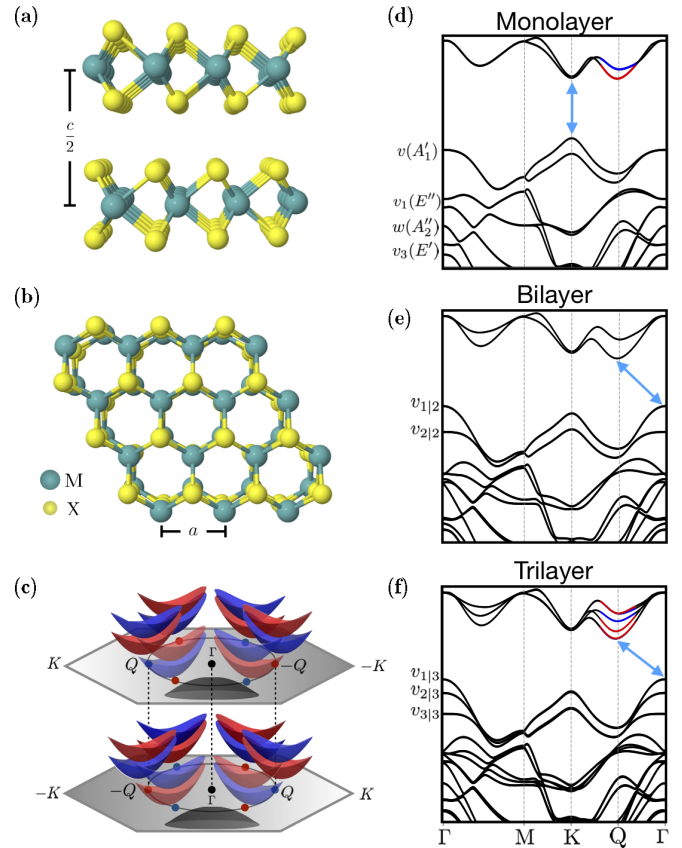


FIG. 2. (a) Crystal structure of a bilayer 2H-stacked TMD (MX_2), the building block of multilayer TMDs, viewed from the side and (b) top. M and X represent the metal and chalcogen atoms, respectively. (c) Brillouin zones of the two monolayers in the 2H-stacked bilayer rotated by 180° relative to each other, and schematics of the band dispersions at the valence band Γ point and conduction band Q point, including the six symmetry-related Q valleys and spin-orbit splitting. (d)–(f) DFT band structures of monolayer, bilayer, and trilayer WS_2 , showing the transition from direct-gap (K - K) monolayer to indirect-gap (Γ - Q) multilayer semiconductor. At the Γ point, we label the different valence bands in the monolayer and the irreducible representations of the D_{3h} point group [26]. The bilayer and trilayer valence subbands are further labeled according to the subscript notation $n|N$, where n is the subband number and N the number of layers. For odd number of layers ($N = 1, 3$), where spin-orbit splitting is present, the conduction subbands near the Q point are colored according to the spin projection quantum number, with red (blue) corresponding to $s = \uparrow$ ($s = \downarrow$), giving a total of $2N$ spin-polarized states. Kramer's doublets are given by $E_s(\mathbf{k}) = E_{-s}(-\mathbf{k})$. For $N = 2$ all bands are spin degenerate, resulting in N doubly degenerate states $E_s(\mathbf{k}) = E_{-s}(\mathbf{k})$.

metal sublayer, forming a trigonal prismatic structure with the metal atom connected to three chalcogens above and below. The monolayer point-group symmetry is D_{3h} , consisting of C_3 rotations, σ_v in-plane mirror reflections, and σ_h out-of-plane mirror reflections. The most common bulk allotrope for these transition-metal dichalcogenides has 2H stacking [31], built by adding subsequent layers rotated by 180° with respect to the center of the hexagon, resulting in a structure where the chalcogen atoms from one layer are directly above or

below metal atoms in the other layer [see Figs. 2(a) and 2(b)]. The interlayer distance $\frac{c}{2}$, with c the out-of-plane lattice constant, is shown in Fig. 2(a), and Fig. 2(b) shows the in-plane lattice constant a . The resulting three-dimensional (3D) layered crystal has a bipartite structure with two monolayers in the unit cell, belonging to the space group $P63/mmc$.

Multilayer TMDs with an even number of layers belong to the point group D_{3d} , which contains spatial inversion ($\mathbf{r} \rightarrow -\mathbf{r}$) but lacks out-of-plane mirror symmetry. The combination of spatial inversion and time-reversal symmetry prescribed at zero magnetic field results in a constraint on the spin splitting of the electronic states for even number of layers $E_s(\mathbf{k}) = E_{-s}(\mathbf{k})$, where s is the spin projection quantum number, such that all states throughout the BZ must be spin degenerate. Similarly to the monolayer case, multilayer films with an odd number of layers belong to the point group D_{3h} , which contains the $z \rightarrow -z$ mirror symmetry σ_h but lacks spatial inversion symmetry. Therefore, s is a good quantum number for which spin degeneracy (present in films with even number of layers) can be lifted by spin-orbit (SO) coupling. While the SO splitting is absent for bands based on p_z and d_{z^2} orbitals at the Γ point, it is substantial near the Q points, leading to the alternation of subband properties. That is, the subbands are spin degenerate for even numbers of layers, resulting in a sixfold degeneracy of dispersion along the ΓK line. For odd number of layers, subband spectra are threefold degenerate, but with $E_s(\mathbf{k}) = E_{-s}(-\mathbf{k})$.

In Figs. 2(d)–2(f) we show how the DFT calculated band structure of WS_2 , representative of all four TMDs, evolves from monolayer to trilayer [15, 17–22] (DFT band structures of all four TMDs can be found in Ref. [32]). The DFT calculations were performed using a plane-wave basis within the local density approximation (LDA), with the QUANTUM ESPRESSO [33] plane-wave self-consistent field (PWSCF) *ab initio* package. We considered the Perdew-Zunger exchange correlation scheme [34], with fully relativistic norm-conserving pseudopotentials, including noncollinear corrections. Pseudopotentials for Mo, W, S, and Se atoms were generated using atomic code *ld1.x* of the PWSCF package [35]. The cutoff energy in the plane-wave expansion was set to 60 Ry, and the BZ sampling of electronic states was approximated using a Monkhorst-Pack uniform k grid of $24 \times 24 \times 1$ for all structures [36]. We adopted a Methfessel-Paxton smearing [37] of 0.005 Ry and set the total energy convergence to less than 10^{-6} eV in all calculations. Spin-orbit coupling was included in all electronic band structure calculations. To eliminate spurious interactions between adjacent supercells, a 20-Å vacuum buffer space was inserted in the out-of-plane direction. We used experimental values for the interlayer separations [38–41] and LDA optimized in-plane lattice constants for all four TMDs [32].

Using WS_2 as an example, Fig. 2 illustrates that a monolayer MX_2 has a direct band gap at the K point of the BZ. The $z \rightarrow -z$ mirror symmetry and lack of inversion symmetry result in SO-split conduction and valence bands, classified by their spin projection quantum number [Fig. 2(d)]. The large SO splitting at the valence band (VB) K point and conduction band (CB) Q point results from their metal d_{xy} and $d_{x^2-y^2}$ orbital compositions. This is in contrast to the CB K point, which is primarily made of metal d_{z^2} orbitals, resulting

in weaker SO splitting [5, 27]. In a 2H-MX_2 bilayer, the combination of spatial inversion and time-reversal symmetry forbids SO splitting, resulting in two spin-degenerate subbands (four bands in total) in the CB and VB, split by the interlayer coupling [Fig. 2(e)]. Additionally, the interlayer coupling shifts the band edges to the Γ point (VB) and to the vicinity of the Q point (CB), making indirect gap semiconductors.

In the trilayer 2H-MX_2 , the valence and conduction band edges remain at the Γ and near the Q points. As shown in Fig. 2(f), the CB subbands are split by SO coupling at the Q point due to the lack of spatial inversion symmetry in the case of odd numbers of layers. The resulting spectrum consists of two SO-split subbands in the middle, and two pairs of nearly spin-degenerate subbands above and below (see Appendix C for details). For the valence subbands, however, SO splitting is forbidden exactly at the Γ point, due to it being its own time-reversal counterpart, resulting in three nearly spin degenerate subbands [exact degeneracy for even N , and spin splitting $E_s(\mathbf{k}) - E_{-s}(\mathbf{k}) \propto k^3$ for odd N]. This trend, which consists of the alternation of SO-split (for odd N) and spin-degenerate (for even N) subbands persists for TMD films with a larger number of layers, and all the same features are present in the spectra of all four 2H-MX_2 shown in Ref. [32]. Finally, we note that the in-plane (2D) carrier dispersions in different subbands $n|N$ (both on the VB and CB sides) are different, which affects the intersubband absorption line shapes, as we discuss in Secs. III and IV.

III. HOLE SUBBANDS IN p -DOPED FEW-LAYER TMDs

Figure 2(d) shows the monolayer valence bands relevant for the multilayer description, based on symmetry and energy considerations. The v and w valence bands are nondegenerate at the Γ point, with the v band composed of the metal d_{z^2} orbital and chalcogen p_z orbitals, whereas the w band is composed of metal and chalcogen p_z orbitals. Bands v_1 and v_3 belong to two-dimensional irreducible representations (Irreps), with

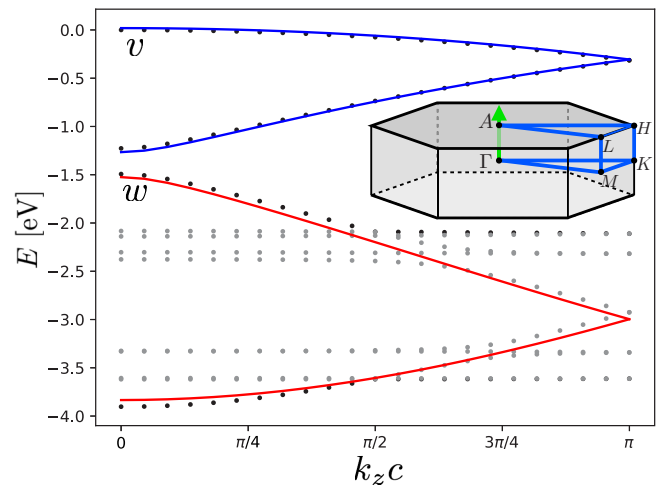


FIG. 3. Bulk dispersion of 2H-stacked WS_2 along the $\overline{\Gamma A}$ line. The DFT data (points) are well fitted by the two-band model (5) (solid lines). The gray points correspond to the v_1 and v_3 valence bands. Inset: the first Brillouin zone of bulk TMDs.

the v_1 band composed of chalcogen p_x, p_y and metal d_{xz}, d_{yz} orbitals, and the v_3 band formed by chalcogen p_x, p_y and metal $d_{xy}, d_{x^2-y^2}$ orbitals [5,26,27]. In the multilayer case, the w and v bands strongly repel as the w band gets closer in energy to the v band. The v_1 and v_3 bands, on the other hand, are weakly split with a narrow spread due to their orbital characters, and are pushed downwards relative to the v -band edge. The two-dimensional Irreps of v_1 and v_3 allow their coupling with the VB being only through SO interactions (see Appendix B). These features involving the symmetry, orbital composition, and proximity of the valence bands, supported by our numerical calculations, indicate that the VB is most strongly hybridized with the w band, while the other valence bands v_1, v_3 , provide corrections in second-order perturbation theory to the model parameters through the action of SO coupling (see Appendix B). Additionally, as pointed out in Sec. II, in two-dimensional 2H- MX_2 crystals the CB and VB are almost spin degenerate at the Γ point, despite the fact that atomic SO coupling in TMD compounds is strong. Therefore, to describe the valence subbands at the Γ point, we construct a spinless two-band model including the v and w bands, fitting the band parameters and interlayer hopping terms to the DFT calculated band structure, where SO coupling

is included implicitly. As indicated in Fig. 2(d), these bands belong to the A'_1 and A'_2 Irreps of the D_{3h} group of the Γ point [26,27], respectively. Therefore, bands v and w are, respectively, even and odd under σ_h transformations, and do not mix in the monolayer case. However, in multilayers, band mixing across consecutive layers is allowed by symmetry.

A. HkpTB for the Γ -point valence band edge

The monolayer dispersions of the valence bands $\sigma = v$ and w are described by isotropic parabolic dispersions with band-dependent effective masses

$$E_\sigma(\mathbf{k}) = E_\sigma^0 - \frac{\hbar^2 k^2}{2m_\sigma}. \quad (1)$$

To construct the multilayer Hamiltonian, we include symmetry-constrained interlayer couplings, given to lowest orders in \mathbf{k} by

$$t_\sigma(\mathbf{k}) = t_\sigma^{(0)} + t_\sigma^{(2)}k^2; \quad t_{vw}(\mathbf{k}) = t_{vw}^{(0)} + t_{vw}^{(2)}k^2, \quad (2)$$

where t_v and t_w are interlayer intraband hopping terms, and t_{vw} couples different bands in two consecutive layers.

The multilayer Hamiltonian is given by

$$\begin{aligned} \hat{H}_{N\Gamma}(\mathbf{k}) = & \sum_{s=\uparrow,\downarrow} \sum_{\sigma=v,w} \sum_{n=1}^{\lceil N/2 \rceil} [E_\sigma(\mathbf{k}) + 2\delta_\sigma + 2\mu_\sigma(\mathbf{k})][a_{ns\sigma}^\dagger(\mathbf{k})a_{ns\sigma}(\mathbf{k}) + \Theta(\frac{N}{2} - n)b_{ns\sigma}^\dagger(\mathbf{k})b_{ns\sigma}(\mathbf{k})] \\ & - \sum_{s=\uparrow,\downarrow} \sum_{\sigma=v,w} [\delta_\sigma + \mu_\sigma(\mathbf{k})][a_{1s\sigma}^\dagger(\mathbf{k})a_{1s\sigma}(\mathbf{k}) + (1 - \frac{\vartheta_N}{2})b_{N/2,s,\sigma}^\dagger(\mathbf{k})b_{N/2,s,\sigma}(\mathbf{k}) + \frac{\vartheta_N}{2}a_{(N+1)/2,s,\sigma}^\dagger(\mathbf{k})a_{(N+1)/2,s,\sigma}(\mathbf{k})] \\ & + \sum_{s=\uparrow,\downarrow} \sum_{\sigma=v,w} \left(\sum_{n=1}^{\lceil N/2 \rceil} t_\sigma(\mathbf{k})\Theta(\frac{N}{2} - n)[a_{ns\sigma}^\dagger(\mathbf{k})b_{ns\sigma}(\mathbf{k}) + \text{H.c.}] + \sum_{n=1}^{\lceil N/2 \rceil - 1} t_\sigma(\mathbf{k})[a_{n+1,s,\sigma}^\dagger(\mathbf{k})b_{ns\sigma}(\mathbf{k}) + \text{H.c.}] \right) \\ & + \sum_{s=\uparrow,\downarrow} \sum_{\sigma=v,w} \sum_{n=1}^{\lceil N/2 \rceil} t_{vw}(\mathbf{k})\Theta(\frac{N}{2} - n)[a_{nsv}^\dagger(\mathbf{k})b_{nsw}(\mathbf{k}) - a_{nsw}^\dagger(\mathbf{k})b_{nv}(\mathbf{k}) + \text{H.c.}] \\ & + \sum_{s=\uparrow,\downarrow} \sum_{\sigma=v,w} \sum_{n=1}^{\lceil N/2 \rceil - 1} t_{vw}(\mathbf{k})[a_{n+1,s,w}^\dagger(\mathbf{k})b_{nsv}(\mathbf{k}) - a_{n+1,s,v}^\dagger(\mathbf{k})b_{nsw}(\mathbf{k}) + \text{H.c.}] \\ & + \sum_{s=\uparrow,\downarrow} \sum_{\sigma=v,w} \sum_{n=1}^{\lceil N/2 \rceil} [U_{2n-1}a_{ns\sigma}^\dagger(\mathbf{k})a_{ns\sigma}(\mathbf{k}) + U_{2n}\Theta(\frac{N}{2} - n)b_{ns\sigma}^\dagger(\mathbf{k})b_{ns\sigma}(\mathbf{k})], \end{aligned} \quad (3)$$

where we have defined $\vartheta_N \equiv 1 - (-1)^N$. $a_{ns\sigma}^{(\dagger)}$ and $b_{ns\sigma}^{(\dagger)}$ annihilate (create) a band- σ electron with spin projection s and in-plane wave vector \mathbf{k} in the odd and even layers of the n th unit cell, respectively. Additional model parameters include the onsite energy corrections δ_v and δ_w , and k -dependent corrections of the form $\mu_\sigma(\mathbf{k}) = \mu_\sigma k^2$, for the v and w bands, respectively, which take into account both the pseudointerlayer potentials, as well as the spin-flip-induced interband-interlayer hopping (Appendix B). For odd N the system has $\lfloor N/2 \rfloor$ complete unit cells and a truncated last unit cell $n = \lceil N/2 \rceil$, where $\lfloor A \rfloor$

and $\lceil A \rceil$ are the floor and ceiling functions, respectively. This case is considered in Eq. (3) through the Heaviside function $\Theta(\frac{N}{2} - n)$, which removes the operators $b_{N/2,\sigma}^{(\dagger)}$ when N is odd. The minus sign in the last row of Eq. (3) for the interband interlayer hoppings (t_{vw}) is due to the opposite parity under $z \rightarrow -z$ of the v and w bands, described in Sec. III. Finally, we include onsite potential energy shifts U_n , for $1 \leq n \leq N$, to take into account the effects of an electric field applied along the TMD film's z axis. Under experimental conditions, such an electric field may originate from a negative back gate, which

in addition dopes the system with a finite hole density ρ_h . This density is related to the potential profile $\{U_n\}$ as [42]

$$U_n = U_1 + ed \sum_{m=2}^N \mathcal{E}_{m-1,m}, \quad n > 1$$

$$\mathcal{E}_{m-1,m} = \frac{2e}{\epsilon_0} \sum_{l=m}^N \rho_l, \quad (4)$$

where e is the (positive) fundamental charge, $d = c/2$ is the interlayer distance, and ρ_l is the electrostatically

induced density of holes in layer l , such that $\rho_h = \sum_{l=1}^N \rho_l$. The factor of 2 in the second equation comes from the spin degeneracy at the Γ point. The potential profile and hole density must be determined self-consistently to satisfy Eq. (4).

Setting $U_n = 0$, we obtain the model parameters in Eq. (3) for each 2H- MX_2 by fitting the results of numerical diagonalization of Eq. (3) to DFT calculations of bulk and few-layer dispersions. For example, the DFT bulk k_z dispersion of WS_2 is shown in Fig. 3 for the $\Gamma\bar{A}$ cut through the 3D BZ. The solid lines in Fig. 3 correspond to the bands of the bipartite Bloch Hamiltonian

$$H_{\Gamma}(\mathbf{k}, k_z) = \begin{pmatrix} E_v(\mathbf{k}) + 2\delta_v + 2\mu_v(\mathbf{k}) & 0 & 2t_v(\mathbf{k}) \cos\left(\frac{k_z c}{2}\right) & 2it_{vw}(\mathbf{k}) \sin\left(\frac{k_z c}{2}\right) \\ 0 & E_w(\mathbf{k}) + 2\delta_w + 2\mu_w(\mathbf{k}) & -2it_{vw}(\mathbf{k}) \sin\left(\frac{k_z c}{2}\right) & 2t_w(\mathbf{k}) \cos\left(\frac{k_z c}{2}\right) \\ 2t_v(\mathbf{k}) \cos\left(\frac{k_z c}{2}\right) & 2it_{vw}(\mathbf{k}) \sin\left(\frac{k_z c}{2}\right) & E_v(\mathbf{k}) + 2\delta_v + 2\mu_v(\mathbf{k}) & 0 \\ -2it_{vw}(\mathbf{k}) \sin\left(\frac{k_z c}{2}\right) & 2t_w(\mathbf{k}) \cos\left(\frac{k_z c}{2}\right) & 0 & E_w(\mathbf{k}) + 2\delta_w + 2\mu_w(\mathbf{k}) \end{pmatrix}, \quad (5)$$

obtained from the model (3). Equation (5) is written in the basis of the v and w bands of layers one and two of the bulk 2H crystal unit cell. The fitted parameters for the four TMDs are given in Tables I and II, and sample comparisons between the HkpTB model and DFT results for WS_2 , representative of all four TMDs, are shown in Fig. 4. Detailed comparisons for few-layer films of all four materials are available in Ref. [32].

Noting that the bulk VB edge is located at the Γ point (Fig. 3), the dispersion near the band edge can be obtained from Eq. (5) as

$$E_{\Gamma}(k_z, \mathbf{k}) \approx -\frac{\hbar^2 k_z^2}{2m_{v,z}} - \frac{\hbar^2 k^2}{2m_{v,xy}} (1 + \zeta k_z^2), \quad (6)$$

where the bulk parameters are given in terms of the HkpTB model parameters:

$$m_{v,z}^{-1} = \frac{\hbar^2}{2d^2} \left(\frac{4t_{vw}^{(0)2}}{\Delta E} + t_v^{(0)} \right) \quad (7a)$$

TABLE I. Model parameters fitted to DFT data for the monolayer valence bands $E_v(\mathbf{k})$ and $E_w(\mathbf{k})$, and bulk valence band dispersion for the four TMDs. The monolayer parameters include the band edges energy difference $E_v^0 - E_w^0$, and the effective masses m_v, m_w given in terms of the free electron mass m_0 . The 3D bulk parameters include the out-of-plane and in-plane effective masses $m_{v,z}$ and $m_{v,xy}$, respectively, and the in-plane dispersion nonlinearity parameter ζ .

	$E_v^0 - E_w^0$ (eV)	m_v (m_0)	m_w (m_0)
	$m_{v,z}$ (m_0)	$m_{v,xy}$ (m_0)	ζ (\AA^2)
MoS ₂	1.75	3.726	0.304
	1.04	0.693	-5.24
MoSe ₂	1.56	5.575	0.505
	1.42	0.786	-5.99
WS ₂	2.08	2.885	0.353
	0.840	0.615	-5.86
WSe ₂	1.81	3.420	0.760
	1.08	0.700	-5.45

is the out-of-plane bulk effective mass, with $d = c/2$ the interlayer distance and $\Delta E = E_v - E_w - 2t_v^{(0)} + 2t_w^{(0)} + 2\delta_v - 2\delta_w$ the bulk gap between the topmost v and lowest w bands at the Γ point,

$$m_{v,xy}^{-1} = \left[1 + \frac{4m_v}{\hbar^2} (t_v^{(2)} - \mu_v) \right] m_v^{-1} \quad (7b)$$

is the in-plane bulk effective mass, and

$$\zeta = -\frac{\hbar^{-2} m_v d^2}{\left[1 + \frac{4m_v}{\hbar^2} (t_v^{(2)} - \mu_v) \right]} \left\{ 2t_v^{(2)} + \frac{4\hbar^2 t_{vw}^2}{\Delta E^2} \frac{m_w - m_v}{m_v m_w} \right. \\ \left. + 16t_{vw} \left(\frac{t_{vw}^{(2)}}{\Delta E} + \frac{t_{vw}}{\Delta E^2} (t_v^{(2)} - t_w^{(2)} + \mu_w - \mu_v) \right) \right\} \quad (7c)$$

is an anisotropic nonlinearity factor. These parameter values, obtained by fitting to DFT calculations, can be found in Table I.

TABLE II. Model parameters fitted to DFT data for the valence band interlayer hopping terms $t_v(\mathbf{k})$, $t_w(\mathbf{k})$, and $t_{vw}(\mathbf{k})$. δ_v , δ_w , μ_v , and μ_w are the onsite energy offsets due to the pseudointerlayer potential and spin-flip coupling terms.

	$t_v^{(0)}$ (eV)	$t_w^{(0)}$ (eV)	$t_v^{(2)}$ (eV \AA^2)	$t_w^{(2)}$ (eV \AA^2)
	$t_{vw}^{(0)}$ (eV)	$t_{vw}^{(2)}$ (eV \AA^2)	δ_v (meV)	δ_w (meV)
			μ_v (eV \AA^2)	μ_w (eV \AA^2)
MoS ₂	-0.333	0.592	1.744	2.684
	0.432	-1.206	-62.18	-41.43
			-0.351	6.770
MoSe ₂	-0.307	0.657	1.830	2.626
	0.453	-1.140	-29.13	-10.85
			-0.261	2.736
WS ₂	-0.322	0.574	1.718	3.205
	0.404	-1.226	-36.98	-48.89
			-0.614	5.834
WSe ₂	-0.291	0.649	1.814	-1.382
	0.4309	-0.049	-25.27	-69.93
			-0.519	0.192

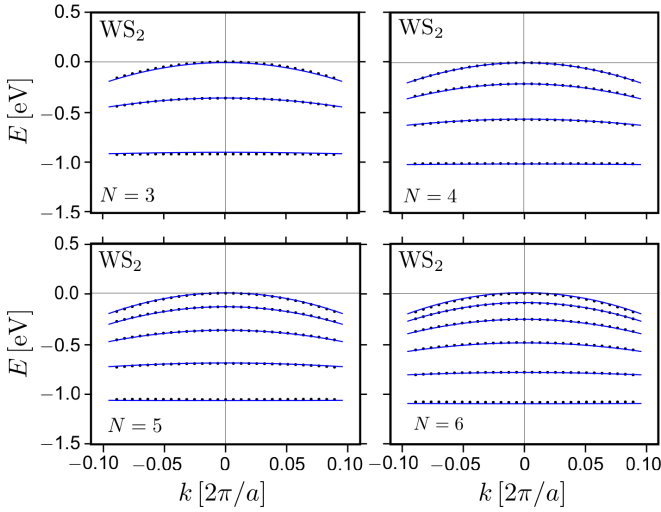


FIG. 4. HkpTB model dispersions (solid lines) fitted to DFT results (points) for the WS₂ valence subbands near the Γ point, representative of all four TMDs. Results are shown for number of layers $N = 3$ to 6. Fittings for all four TMDs can be found in Ref. [32].

Then, the subband energies and dispersions in TMD films with $N \gg 1$ can be analyzed by quantizing hole states with dispersions described by Eq. (6) in a slab of thickness $L = Nd$. When doing so, one has to complement Eq. (6) with the general Dirichlet-Neumann boundary condition for the standing waves of holes at both film surfaces

$$[\pm v d \partial_z \psi(z) + \psi(z)]_{z=\pm \frac{L}{2}} = 0, \quad (8)$$

where the \pm correspond to the top and bottom layers, respectively, and v is a dimensionless parameter. Assuming a solution of the form $\psi(z) = u e^{i k_z z} + v e^{-i k_z z}$, one finds from Eq. (8) that k_z in Eq. (6) obeys

$$L k_z + 2 \arctan(v k_z d) = \pi n, \quad (9)$$

where the integer n is the subband index. For large number of layers and for subbands near the band edge, $k_z \sim \frac{1}{L} \ll \frac{1}{d}$, and $\arctan(v k_z d) \approx v k_z d$, so that we can approximate

$$k_z \approx \frac{\pi n}{d(N + 2v)}, \quad (10)$$

leading to the subband energies and dispersions

$$E_{n \ll N|N}(\mathbf{k}) = -\frac{\hbar^2}{2m_{v,z}} \frac{\pi^2 n^2}{d^2(N + 2v)^2} - \frac{\hbar^2 k^2}{2m_{v,xy}} \left[1 + \frac{\zeta \pi^2 n^2}{d^2(N + 2v)^2} \right]. \quad (11)$$

The large- N asymptotics of the separation between the lowest two subbands, $|E_{1|N} - E_{2|N}|$, was used to determine the value of the boundary parameter v for holes in each TMD, resulting in $v \approx 0$ for MoS₂ and MoSe₂, $v = 0.11$ for WS₂, and $v = 0.007$ for WSe₂, using the dispersions and lowest intersubband splittings shown in Figs. 4 and 5(a). The good agreement between the full HkpTB model and the asymptotic analysis shown in Fig. 5(a) enables us to describe the main intersubband transition $1|N \rightarrow 2|N$ in p -doped N -layer 2H-

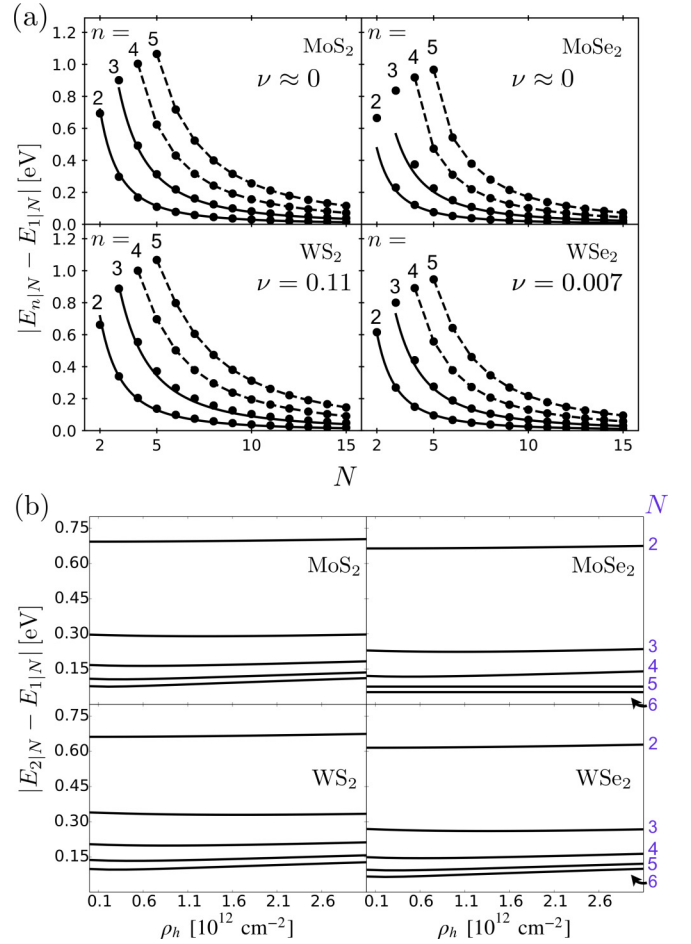


FIG. 5. (a) Energy spacings between the first and n th valence subband ($n = 2$ to 5) for the four TMDs, as a function of the number of layers N . The v parameter corresponding to each TMD is given in each panel. The solid lines for the first two transitions are obtained using Eq. (11), showing a good fit between the model and DFT. (b) $1|N \rightarrow 2|N$ transition energy as a function of the hole density ρ_h . Each curve corresponds to the value of N indicated on the right.

MX_2 as

$$|E_{1|N} - E_{2|N}| = \frac{3\pi^2 \hbar^2}{2m_{v,z} d^2 (N + 2v)^2}. \quad (12)$$

Furthermore, the hole subband effective masses

$$m_{n|N}^{-1} = m_{v,xy}^{-1} \left[1 + \frac{\zeta \pi^2 n^2}{d^2 (N + 2v)^2} \right], \quad (13)$$

obtained from Eq. (11), describe well the subband dependence of the in-plane masses, as seen in Fig. 5(a).

Figure 5(b) shows the effects of a doping-induced potential profile in the film on the first subband transition energy $|E_{2|N} - E_{1|N}|$, as a function of the total gate-induced hole density ρ_h . Results are shown for all four TMDs with film thicknesses of $N = 2$ to 6 layers, up to moderate doping levels. Following a slight decrease for weak doping, the transition energies grow monotonically, but with only a weak blue-shift.

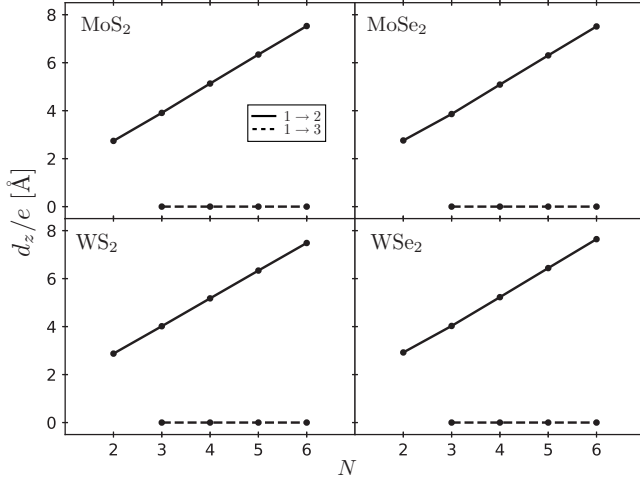


FIG. 6. Out-of-plane dipole moment matrix elements for the VB subbands, for the first two intersubband transitions $1 \rightarrow 2$ (solid line) and $1 \rightarrow 3$ (dashed line).

B. Selection rules for intersubband transitions, and dispersion-induced line broadening

Next, we use the model developed above for the description of hole subbands to study intersubband optical transitions, electron-phonon relaxation, and absorption line shapes of IR/FIR light. The optical transition amplitude between two given subbands n and n' is determined by the out-of-plane dipole moment

$$d_z^{n,n'}(\mathbf{k}) = e \langle n, \mathbf{k} | z | n', \mathbf{k} \rangle$$

$$= e \sum_{j=1}^N \sum_{\sigma=v,w} z_j C_{n,j,\sigma}^*(\mathbf{k}) C_{n',j,\sigma}(\mathbf{k}), \quad (14)$$

where N is the total number of layers, z_j denotes the z coordinate of layer j , and $C_{n,j,\sigma}(\mathbf{k})$ are the components of the n th subband eigenstate. The calculated dipole moment matrix element for the first two intersubband transitions is plotted in Fig. 6 as a function of the number of layers. The selection rules for intersubband transitions driven by out-of-plane polarized light are determined by the odd parity of z under both spatial inversion and mirror reflection (σ_h). The subband states for even and odd number of layers also have a definite parity under spatial inversion and mirror reflection, respectively, due to the crystal symmetry. Therefore, intersubband transitions between same parity subbands are forbidden, as shown in Fig. 6 for the first two intersubband transitions. All this makes the $1|N \rightarrow 2|N$ transition the dominant feature in the IR/FIR absorption by thin TMD films.

The intersubband absorption line shape is affected by the difference between the effective masses of subbands $1|N$ and $2|N$. The lighter in-plane hole mass in the initial state ($1|N$ subband) as compared to the final state ($2|N$ subband) spreads the absorption spectrum toward lower energies. Heavy p doping of the TMD film or Boltzmann distribution of the holes in the case of light p doping sets the lower limit for the line width of the $1|N \rightarrow 2|N$ absorption line, which we call

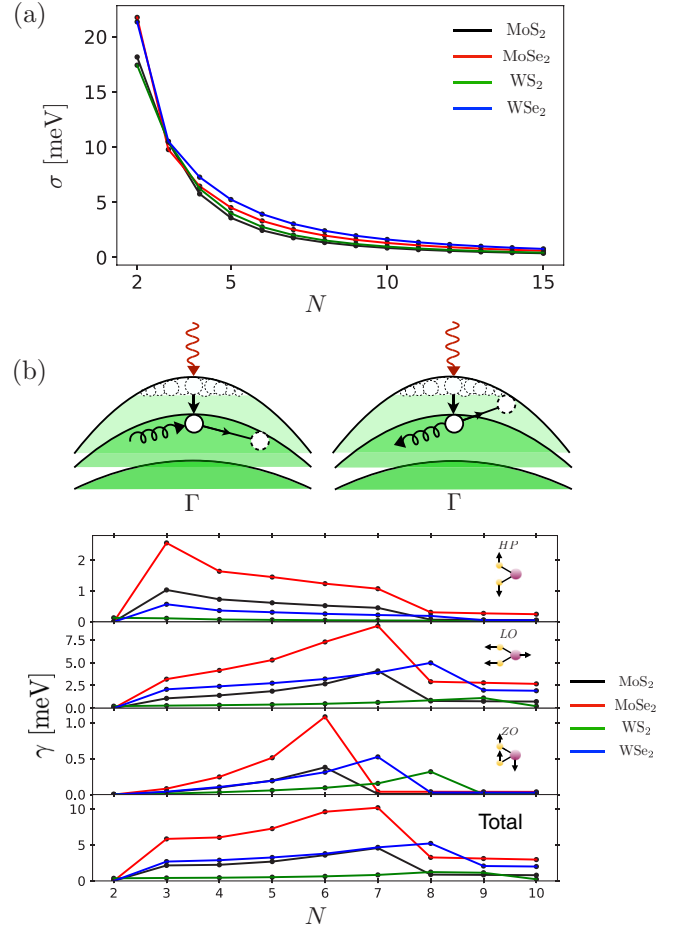


FIG. 7. (a) Absorption line widths for VB subbands at room temperature (300 K) as a function of number of layers for the four TMDs, considering only DOS broadening. (b) Phonon-induced broadening at room temperature ($T = 300$ K) due to intersubband emission and intrasubband absorption of optical phonon modes (top to bottom) HP, LO, and ZO, for the four TMDs as a function of number of layers N , with the combined broadening shown in the bottom panel.

the density of states (DOS) broadening

$$\sigma = \left(1 - \frac{m_{1|N}}{m_{2|N}}\right) \max\{\epsilon_F, k_B T\} \log 2. \quad (15)$$

Here, k_B is the Boltzmann constant, T is the temperature, and m_1, m_2 are the effective masses of the first and second subbands. This limit for the line width is illustrated in Fig. 7(a) for N -layer $2H-MX_2$ at room temperature. We note here that DOS broadening is similar to the inhomogeneous broadening, in the sense that it can be overcome by placing the TMD film inside an optical resonator that would select intersubband modes with particular values of in-plane momentum \mathbf{k} .

C. Broadening due to electron-phonon intrasubband and intersubband relaxation

In contrast to the elastic DOS broadening, phonon-induced intrasubband and intersubband relaxation broaden the absorption line in a way that cannot be avoided by a clever choice of the electromagnetic environment. Below, we consider emission

TABLE III. Electron-phonon coupling parameters for LO, HP, and ZO phonon modes. ω_{HP} , ω_{LO} , and ω_{ZO} are the HP, LO, and ZO mode energies; ρ is the mass density; D_v , D_c are the valence and conduction deformation potentials; Z , Z_z are the in-plane and out-of-plane Born effective charges; r_* is the screening length; M_r/M is the ratio of the reduced mass of the metal and chalcogens to the total unit-cell mass; and A is the unit-cell area.

	$\hbar\omega_{\text{HP}}$ (meV)	$\hbar\omega_{\text{LO}}$ (meV)	$\hbar\omega_{\text{ZO}}$ (meV)	ρ (g/cm ²)	D_v (eV/Å)	D_c (eV/Å)	Z	Z_z	r_* (Å)	M_r/M	A (Å ²)
MoS ₂	51	49	59	3.1×10^{-7}	3.5	7.1	1.08	0.1	41	0.24	8.65
MoSe ₂	30	37	44	4.5×10^{-7}	3.8	7.8	1.8	0.15	52	0.249	9.37
WS ₂	52	44	55	4.8×10^{-7}	1.5	3.4	0.47	0.07	38	0.29	8.65
WSe ₂	31	31	39	6.1×10^{-7}	2.2	2.7	1.08	0.12	45	0.25	9.37

and absorption of homopolar (HP), longitudinal (LO), and out-of-plane (ZO) optical phonons, which we assume to be dispersionless. This choice is motivated by the fact that these are the strongest coupled modes in TMDs, as established by earlier studies [28,43]. Also, we take phonon modes of few-layer films as independent and degenerate. This approximation is justified by the fact that splittings due to hybridization between layers are much smaller than the monolayer phonon frequency [44].

The hole-phonon couplings for a phonon in mode $\mu = \text{HP, LO, or ZO}$ in layer j , interacting with a hole in layer i , are given by (see Appendices D and E)

$$g_{\text{HP}}^{j,i}(\mathbf{q}) = \delta_{ij} \sqrt{\frac{\hbar}{2\rho\omega_{\text{HP}}}} D_v, \quad (16a)$$

$$g_{\text{LO}}^{j,i}(\mathbf{q}) = \sqrt{\frac{\hbar}{2\rho\frac{M_r}{M}\omega_{\text{LO}}}} \frac{2\pi i e^2 Z (-1)^j}{A(1+r_*q)} e^{-qd|i-j|}, \quad (16b)$$

$$g_{\text{ZO}}^{j,i}(\mathbf{q}) = \sqrt{\frac{\hbar}{2\rho\frac{M_r}{M}\omega_{\text{ZO}}}} \frac{2\pi e^2 Z_z}{A} e^{-qd|i-j|} \frac{i-j}{|i-j|}, \quad (16c)$$

where ω_μ denotes the corresponding phonon frequency; ρ is the mass density of the material; D_v is the deformation potential in the valence band; A is the unit-cell area; M and M_r are the total unit-cell mass and reduced mass of the metal and two chalcogens, respectively; Z and Z_z are the in-plane and out-of-plane Born effective charges, respectively; and r_* is the screening length in the material. The various parameters taken from Refs. [28,43,45,46] are given in Table III.

The phonon-induced broadening is determined by the lifetime of the hole in the excited subband state, which includes contributions from intersubband relaxation due to emission (low and high temperature) and intrasubband absorption (high temperature) [Fig. 7(b)]. We note that intrasubband emission contributions are thermally activated, since they require carriers to be thermally excited to energies higher than the corresponding phonon energy. The typical energy of thermally distributed carriers at room temperature is $\frac{1}{2}k_B T \sim 13$ meV, whereas the phonon energies are of order 30–50 meV (Table III), making this process irrelevant. Similarly, the process involving intersubband absorption from the second subband to the third is suppressed by the larger intersubband spacings, as compared to the phonon energies and the first intersubband spacings for $N \lesssim 10$, and therefore will not be considered.

The phonon-induced broadening is accounted for by

$$\gamma = 2\pi \sum_{\mu, \mathbf{q}, j} \left| \sum_i \sum_{\sigma=v,w} g_\mu^{j,i}(\mathbf{q}) C_{n,i,\sigma}^*(\mathbf{q}) C_{m,i,\sigma}(0) \right|^2 \times \{ [1 + n_T(\hbar\omega_\mu)] \delta[E_m(0) - E_n(\mathbf{q}) - \hbar\omega_\mu] + \delta_{nm} n_T(\hbar\omega_\mu) \delta[E_m(0) - E_m(\mathbf{q}) + \hbar\omega_\mu] \}, \quad (17)$$

where the sums are over the phonon modes $\mu = \text{HP, LO, ZO}$, the phonon wave vector \mathbf{q} , and the layer number $1 \leq j \leq N$. $C_{n,i,\sigma}$ are the components of the n th subband eigenstate on layer i in band σ , and $n_T(\hbar\omega_\mu)$ is the Bose-Einstein distribution for a phonon in mode μ at temperature T . The first term in curly brackets describes intersubband phonon emission, whereas the second term describes intrasubband phonon absorption.

The resulting phonon-induced broadenings at room temperature are shown in Fig. 7(b). The main contribution comes from intersubband relaxation, with intrasubband absorption suppressed by the phonon occupation number. The intersubband LO phonon contribution dominates the broadening due to the strong coupling attributed to the large in-plane Born effective charge, and the long-range nature of the coupling. The reduced broadening for $N = 2$ is due to the large intersubband spacing, which suppresses intersubband relaxation, and the fact that the second subband is almost flat, which suppresses intrasubband absorption. The peaks in the broadenings for certain numbers of layers correspond to near resonances between the phonon energies and the intersubband spacings. Phonon broadening is seen to be most detrimental for MoSe₂ in particular, and in general for all TMDs with seven or eight layers. Beyond this number of layers, the phonon energies become larger than the intersubband spacings, thus preventing intersubband relaxation, however, intrasubband absorption is still present and dominates for $N > 7$. Finally, we note that the broadening values are found to be smaller than those observed in III-V quantum wells [30], implying a weaker detrimental effect on the absorption/emission line shape in these materials.

D. Room-temperature absorption spectrum in p -doped TMD films

The cumulative effect of inelastic (e-ph) and elastic (DOS) broadening of the intersubband $1|N \rightarrow 2|N$ absorption spectra of lightly p -doped TMD films is described by

$$I(\hbar\omega) = \frac{4\pi}{\hbar} |E_z(\hbar\omega)|^2 \sum_{\mathbf{k}} |d_z^{1,2}(\mathbf{k})|^2 f_T(\mathbf{k}) \times \frac{\gamma/\pi}{[E_1(\mathbf{k}) - E_2(\mathbf{k}) - \hbar\omega]^2 + \gamma^2}, \quad (18)$$

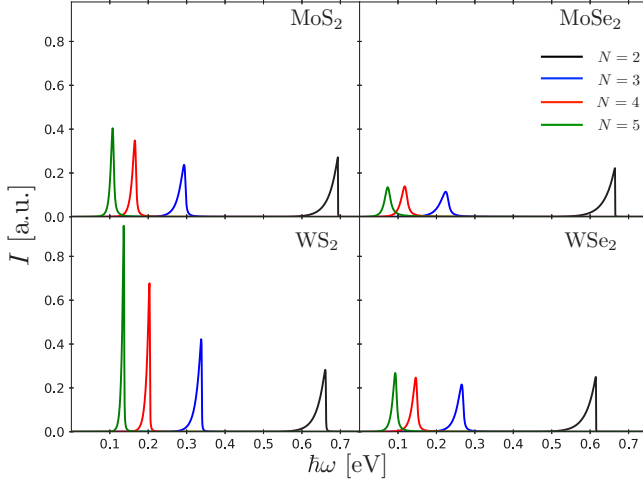


FIG. 8. Optical absorption lines for $N = 2$ to 5 layers of lightly p -doped MoS₂, MoSe₂, WS₂, and WSe₂ at room temperature ($T = 300$ K).

where $f_T(\mathbf{k})$ is the Fermi function for hole occupation in the lowest subband corresponding to hole density n_h , and temperature T (we assume that all higher-energy hole subbands are empty). The resulting absorption spectra at room temperature for the four TMDs with different number of layers are shown in Fig. 8. The spectra show the combination of DOS broadening, which produces a tail towards lower photon energies, with the phonon-induced broadening, most relevant for $N > 2$, which gives a small tail towards higher energies, making the lines more symmetric and reducing their amplitudes. The smaller phonon couplings in WS₂ result in tall, narrow, and asymmetric line shapes, with intensity increasing with the number of layers, reflecting the growing dipole matrix element. This is in contrast to MoSe₂, where the larger phonon-induced broadening results in smaller and more symmetric peaks for $N > 2$.

IV. ELECTRON SUBBANDS IN n -DOPED FEW-LAYER TMDs

A. HkpTB for the conduction band near the Q point

The conduction band edges in monolayer MoS₂, MoSe₂, WS₂, and WSe₂ are located at the K points, but accompanied by local dispersion minima that appear near the six inequivalent points $\tau\mathbf{Q}$, $\tau C_3\mathbf{Q}$, and $\tau C_3^2\mathbf{Q}$, where $\tau = \pm 1$, and $\mathbf{Q} = \frac{2\pi}{3a}\hat{x}$ is the midpoint between Γ and \mathbf{K} (a is the lattice constant). For a given value of τ , there are three valleys connected by C_3 rotations about the BZ center [Fig. 2(c)], such that we need only describe the dispersion near the two points $\tau\mathbf{Q}$, which are related by time reversal.

For spin projection s , the monolayer dispersion near the $\tau\mathbf{Q}$ valley is given by [27]

$$E_s^\tau(\mathbf{k}) = \frac{\hbar^2(k_x - q_s^\tau)^2}{2m_{x,s}^\tau} + \frac{\hbar^2 k_y^2}{2m_{y,s}^\tau} + E_0 + \tau s \Delta_0, \quad (19)$$

where $m_{x,s}^\tau$ and $m_{y,s}^\tau$ are effective masses; E_0 is a constant energy shift; $2\Delta_0$ is the spin-orbit splitting between the spin-up and -down band edges; and q_s^τ is the band-edge momentum relative to the valley along the \hat{x} axis. From time-reversal symmetry we obtain the dispersion for the opposite valley as $E_s^\tau(\mathbf{k}) = E_{-s}^{-\tau}(-\mathbf{k})$, which requires ($\alpha = x, y$) $m_{\alpha,s}^\tau = m_{\alpha,-s}^{-\tau}$ and $q_s^\tau = -q_{-s}^{-\tau}$.

As described in Sec. II, the 2H-stacked bilayer consists of subsequent layers rotated by 180° with respect to each other. In reciprocal space, this means that a conduction band state of spin projection s and momentum $\tau\mathbf{Q} + \mathbf{k}$ of the first layer will hybridize with its in-plane inversion partner of spin s and momentum $-\tau\mathbf{Q} - \mathbf{k}$ in the second one [Fig. 2(c)]. The multilayer Hamiltonian for the conduction subbands about $\tau\mathbf{Q}$ is given by

$$\begin{aligned} H_{NQ}^\tau(\mathbf{k}) = & \sum_{n=1}^{\lceil N/2 \rceil} \sum_{s=\uparrow,\downarrow} [E_s^\tau(\mathbf{k}) + (\delta_{n,1} + \delta_{n,\lceil N/2 \rceil})\delta E] [a_{n\tau s}^\dagger(\mathbf{k})a_{n\tau s}(\mathbf{k}) + \Theta(\frac{N}{2} - n)b_{n,-\tau,-s}^\dagger(-\mathbf{k})b_{n,-\tau,-s}(-\mathbf{k})] \\ & + \sum_{n=1}^{\lceil N/2 \rceil} \sum_{s=\uparrow,\downarrow} t_\tau(\mathbf{k})\Theta(\frac{N}{2} - n)[b_{n,-\tau,-s}^\dagger(-\mathbf{k})a_{n\tau s}(\mathbf{k}) + \text{H.c.}] + \sum_{n=1}^{\lceil N/2 \rceil - 1} \sum_{s=\uparrow,\downarrow} t_\tau^*(\mathbf{k})[b_{n,-\tau,-s}^\dagger(-\mathbf{k})a_{n+1,\tau,s}(\mathbf{k}) + \text{H.c.}] \\ & + \sum_{n=1}^{\lceil N/2 \rceil - 1} \sum_{s=\uparrow,\downarrow} t' [a_{n+1,\tau,s}^\dagger(\mathbf{k})a_{n\tau s}(\mathbf{k}) + b_{n+1,-\tau,s}^\dagger(-\mathbf{k})b_{n,-\tau,s}(-\mathbf{k})] \\ & + \sum_{n=1}^{\lceil N/2 \rceil} \sum_{s=\uparrow,\downarrow} [U_{2n-1} a_{n\tau s}^\dagger(\mathbf{k})a_{n\tau s}(\mathbf{k}) + U_{2n}\Theta(\frac{N}{2} - n)b_{n,-\tau,-s}^\dagger(\mathbf{k})b_{n,-\tau,-s}(\mathbf{k})], \end{aligned} \quad (20)$$

where $a_{n,\tau,s}^\dagger(\mathbf{k})$ and $b_{n,\tau,s}^\dagger(\mathbf{k})$ annihilate (create) electrons of spin projection s , in-plane wave vector \mathbf{k} and valley quantum number τ , on the odd and even layers of the n th bulk unit cell. The alternation of spin indices and hopping terms are a result of 2H stacking. The model is parametrized by the terms in $t_\tau(\mathbf{k})$ given in Eq. (21), the interlayer pseudopotential δE ,

implemented as an onsite energy shift at the boundary layers, and the next-nearest-neighbor hopping t' included to improve the fitting to DFT bands. The interlayer hopping has the form (see Appendix A)

$$t_\tau(\mathbf{k}) = t_0 + \tau t_1 k_x + i u_1 k_y + t_2 k_x^2 + u_2 k_y^2, \quad (21)$$

TABLE IV. Monolayer and bulk conduction band parameters fitted to DFT calculations of the four TMDs. The effective masses are given in terms of the free electron mass m_0 . The band-edge energy E_0 is given relative to the valence band edge at the Γ point, and $2\Delta_0$ is the spin-orbit splitting at the Q point. The monolayer parameters include the effective masses in the x and y directions for the spin-split bands, and the band minima offsets q_\downarrow and q_\uparrow . The conduction band bulk dispersion parameters include the in-plane effective masses $m_{c,x}, m_{c,y}$, and out-of-plane mass $m_{c,z}$; band minima offsets κ_0 and β , and in-plane dispersion nonlinearity parameters ζ_x and ζ_y .

	$m_{x,\uparrow} (m_0)$	$m_{y,\uparrow} (m_0)$	$q_\uparrow (10^{-3} \text{\AA}^{-1})$	$m_{x,\downarrow} (m_0)$	$m_{y,\downarrow} (m_0)$	$q_\downarrow (10^{-3} \text{\AA}^{-1})$	E_0 (eV)	$2\Delta_0$ (meV)
	$m_{c,z} (m_0)$	$m_{c,x} (m_0)$	$m_{c,y} (m_0)$	$\zeta_x (\text{\AA}^2)$	$\zeta_y (\text{\AA}^2)$	$\kappa_0 (\text{\AA}^{-1})$	$\beta (10^{-4} \text{\AA})$	
MoS ₂	0.595	1.035	20.49	0.666	1.105	7.16	1.994	67.0
	0.525	0.550	0.735	-3.90	-7.94	0.0456	-1.3	
MoSe ₂	0.583	1.060	54.21	0.518	1.106	26.93	1.891	21.0
	0.500	0.510	0.760	-4.65	-4.26	0.0663	0.32	
WS ₂	0.529	0.722	13.74	0.763	0.892	-20.65	2.059	254
	0.510	0.528	0.596	-4.30	-4.12	0.0344	0.53	
WSe ₂	0.468	0.753	49.63	0.676	0.908	1.88	1.94	214
	0.466	0.479	0.608	-4.19	-5.80	0.0599	-0.9	

up to second order in the in-plane crystal momentum. Given the lack of σ_h symmetry for even N , the spin projection s is, strictly speaking, not a good quantum number, and spin mixing is allowed. This is discussed in Appendix A. However, using an expansion about the Q point in our DFT results shows that spin mixing is much weaker [47] than $t_\tau(\mathbf{k})$, and can be neglected. We also found u_1 to be several orders of magnitude smaller than t_1 ; as a result, we consider $t_\tau(\mathbf{k})$ to be real.

Finally, in the last term of Eq. (20) we take into account electrostatic doping effects through the layer-dependent potential energy U_n ($1 \leq n \leq N$) [42]:

$$U_n = U_1 + ed \sum_{m=2}^N \mathcal{E}_{m-1,m}, \quad n > 1$$

$$\mathcal{E}_{m-1,m} = \frac{3e}{\epsilon_0} \sum_{l=m}^N \sum_{\tau=\pm 1} \sum_{s=\uparrow,\downarrow} \rho_l^{s\tau}. \quad (22)$$

Here, $\rho_l^{s\tau}$ is the electron (number) density induced in layer l belonging to the spin- s subbands in valley τ . The factor of 3 in the second equation comes from the valley degeneracy, which is preserved even in the presence of an out-of-plane electric field.

In the bulk limit, and in the absence of external electric fields ($U_n = 0$), we have the bipartite Hamiltonian

$$H_Q^\tau(\mathbf{k}, k_z) = \epsilon_0(\mathbf{k}, k_z) s_0 \pi_0 + \tau \Delta(\mathbf{k}) s_3 \pi_3$$

$$+ 2t_\tau(\mathbf{k}) \cos\left(\frac{k_z c}{2}\right) s_0 \pi_1,$$

$$\epsilon_0(\mathbf{k}, k_z) = \frac{E_\uparrow^+(\mathbf{k}) + E_\downarrow^+(\mathbf{k})}{2} + 2t' \cos(k_z c),$$

$$\Delta(\mathbf{k}) = \frac{E_\uparrow^+(\mathbf{k}) - E_\downarrow^+(\mathbf{k})}{2}, \quad (23)$$

where $\Delta(\mathbf{k})$ is the \mathbf{k} -dependent monolayer spin-orbit splitting for wave vector \mathbf{k} measured relative to the Q point; s_i and π_i ($i = 0$ to 3) are Pauli matrices acting on the spin and layer degrees of freedom, respectively, and s_0 and π_0 are the identity in their corresponding subspaces. The model parameters for

the four TMDs were fitted to the DFT calculated monolayer and 3D bulk dispersions, and are presented in Tables IV and V. A sample bulk fitting is shown in Fig. 9 for WS₂, along the path defined by $k_x = k_y = 0$ (Q point) and $k_z \in [0, \pi/c]$, with the solid line corresponding to the model (23). A sample comparison between our HkpTB model to DFT results for WS₂ few-layer structures, representative of all four TMDs, is shown in Fig. 10. Detailed comparisons for few-layer films of all four materials are available in Ref. [32].

As discussed in Sec. II, the global symmetry alternation between σ_h for odd N , and spatial inversion symmetry for even N , results in the striking qualitative differences between the cases with even and odd number of layers in Fig. 10. The twofold spin degeneracy observed for even N is a consequence of spatial inversion and time-reversal symmetry, resulting in $E_s^\tau(\mathbf{k}) = E_{-s}^\tau(\mathbf{k})$. By contrast, σ_h mirror symmetry for N odd makes s a good quantum number, while the lack of inversion symmetry allows for spin-orbit splitting. Notice also that the two middle spin-split subbands remain fixed for all odd values of N , while the rest of the bands are nearly spin degenerate. As discussed in Appendix C, these features can be traced back to the SO splitting in the monolayer case, and the particular form of Hamiltonians $H_{NQ}^\tau(\mathbf{k})$ for odd N .

Expanding the lowest eigenvalue of Eq. (23) for valley τ about $k_z = 0$, corresponding to the bulk conduction band edge

TABLE V. Model parameters fitted to DFT data for the conduction band interlayer hopping terms. δE is an energy offset for the first and last layers of the structure that accounts for surface effects.

	t_0 (eV)	t_1 (eV\AA)	t_2 (eV\AA ²)
	t' (meV)	u_2 (eV\AA ²)	δE (meV)
MoS ₂	0.203	0.213	0.0419
	12.7	-0.662	8.90
MoSe ₂	0.215	0.180	-0.145
	20.5	-0.447	-4.29
WS ₂	0.210	0.233	-0.123
	5.24	-0.864	-3.95
WSe ₂	0.211	0.209	0.231
	9.54	-0.797	4.21

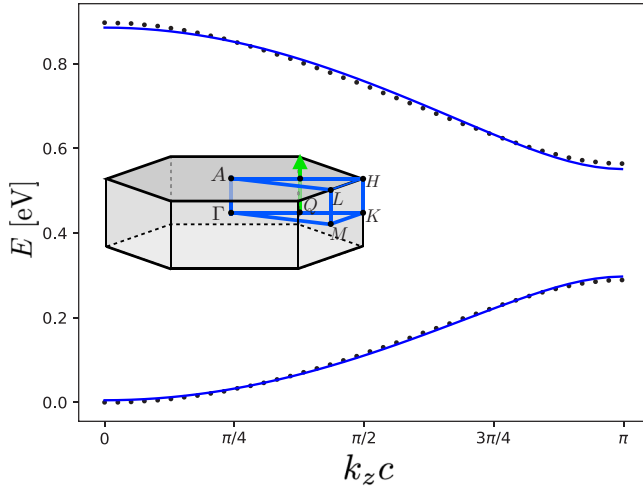


FIG. 9. Bulk dispersion of 2H-stacked WS_2 along the Brillouin zone path \overline{QA} , defined by $k_x = k_y = 0$ and $k_z \in [0; \pi/c]$, where k_x and k_y are measured relative to the Q point, as shown in the inset. DFT data (points) are well fitted by the model (23) (solid line). Inset: the first Brillouin zone of bulk TMDs.

(Fig. 9), the dispersion can be written as

$$E_Q^\tau(\mathbf{k}, k_z) \approx \frac{\hbar^2}{2m_{c,x}} (k_x - \tau[\kappa_0 - \beta k_z^2])^2 (1 + \zeta_x k_z^2) + \frac{\hbar^2 k_y^2}{2m_{c,y}} (1 + \zeta_y k_z^2) + \frac{\hbar^2 k_z^2}{2m_{c,z}} + E_Q^0, \quad (24)$$

where $m_{c,z}$ is the out-of-plane bulk effective mass; $m_{c,x}$, $m_{c,y}$ are the in-plane effective masses in the x and y directions,

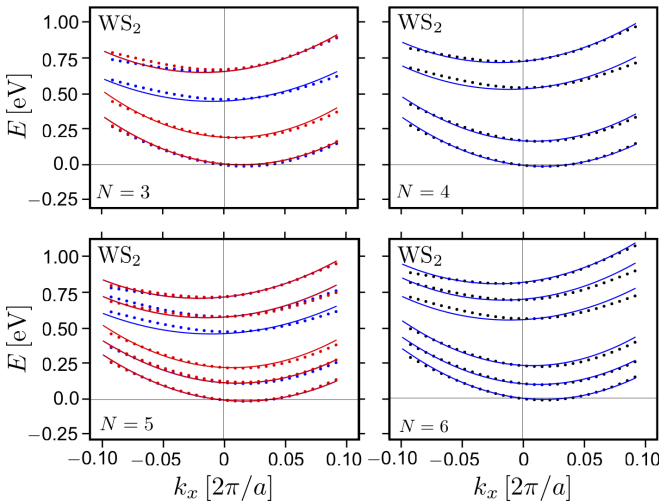


FIG. 10. HkpTB model dispersions (solid lines) fitted to DFT results for the WS_2 conduction subbands (points) near the Q point ($k_x = 0$), representative of all four TMDs. Results are shown for number of layers $N = 3$ to 6. For odd N , line and point colors indicate subbands with different spin projections, with blue (red) corresponding to spin down (spin up). For even N , spin-up and -down subbands are degenerate, and shown with black dots. Fittings for all four TMDs can be found in Ref. [32].

respectively; ζ_x, ζ_y are anisotropic non-linearity factors; κ_0 and β account for the band minimum offset from the Q point along the \hat{x} direction; and E_Q^0 is a constant energy shift. These constants are related to our HkpTB model parameters through the expressions [see Eq. (19)]

$$m_{c,x} = \frac{2m_{x,\uparrow}^\tau m_{x,\downarrow}^\tau}{m_{x,\uparrow}^\tau + m_{x,\downarrow}^\tau}, \quad (25a)$$

$$m_{c,y} = \frac{2m_{y,\uparrow}^\tau m_{y,\downarrow}^\tau}{m_{y,\uparrow}^\tau + m_{y,\downarrow}^\tau}, \quad (25b)$$

$$m_{c,z} = \frac{\hbar^2}{8d^2} \left[\frac{t_0^2}{4\Delta_0} \left(1 - \frac{t_1^2}{t_1^2 + 2t_0t_1} \right) - t' + \frac{t_1^2 + 2t_0t_2}{4\Delta_0} \left(\kappa_0 + \frac{t_0t_1}{t_1^2 + 2t_0t_2} \right)^2 \right]^{-1}, \quad (25c)$$

$$\kappa_0 = \frac{m_{x,\uparrow}^+ q_\downarrow^+ + m_{x,\downarrow}^+ q_\uparrow^+}{m_{x,\uparrow}^+ + m_{x,\downarrow}^+}, \quad (25d)$$

$$\beta = \frac{2m_{c,x} d^2 t_1^2 + 2t_0t_2}{\hbar^2 \Delta_0} \left(\kappa_0 + \frac{t_0t_1}{t_1^2 + 2t_0t_2} \right), \quad (25e)$$

$$\zeta_x = \frac{2m_{c,x} d^2 t_1^2 + 2t_0t_2}{\hbar^2 \Delta_0}, \quad (25f)$$

$$\zeta_y = \frac{4m_{c,y} d^2 t_0t_2}{\hbar^2 \Delta_0}, \quad (25g)$$

$$E_Q^0 = E_0 - 2\Delta_0 + \frac{\hbar^2 (q_\uparrow^\tau + q_\downarrow^\tau)^2}{4 m_{x,\uparrow}^\tau + m_{x,\downarrow}^\tau} + 2t'. \quad (25h)$$

Similarly to the subbands on the valence band side (Sec. III), the conduction subbands in TMD films with $N \gg 1$ can be analyzed by quantizing the electron states in a slab of finite thickness $L = Nd$, with dispersions described by Eq. (24). However, note that the coefficients of Eqs. (25a)–(25h) are independent of spin projection and valley, and thus not representative of the odd- N case. This is a consequence of the explicit inversion symmetry of the bulk model (23). Nonetheless, the SO splitting resulting from the lack of inversion symmetry and the presence of σ_h symmetry in a system with odd N can be introduced through the TMD quantum well boundary conditions.

The unit cell for 2H crystals contains two layers, which below we label A and B [see Eq. (20)]. For odd N , inversion symmetry is broken in opposite ways for the two layers in the unit cell, given that, as discussed in Sec. I, they are rotated by 180° with respect to each other. This results in different boundary conditions for electrons at a given termination of the TMD film, depending on whether the final layer is of type A or B. This generalizes the boundary conditions used for the valence band at the Γ point [Eq. (8)] to

$$\left[\pm (v_0 + s\tau v_1) d \partial_z \psi_s^\tau(z) + \psi_s^\tau(z) \right]_{z=\pm \frac{L}{2}} = 0, \quad (26a)$$

for the boundary at $z = \pm L/2$ when the film terminates on an A layer, and

$$\left[\pm (v_0 - s\tau v_1) d \partial_z \psi_s^\tau(z) + \psi_s^\tau(z) \right]_{z=\pm \frac{L}{2}} = 0, \quad (26b)$$

when the final layer at position $z = \pm L/2$ is of type B. Here, $v_0, v_1 \ll N$ are dimensionless parameters. This results in spin- and valley-dependent quantization conditions

$$\kappa_{z,n|N}^{s,\tau} \approx \frac{\pi n}{d[N + 2v_0 + s\tau v_1 \vartheta_N]}, \quad (27)$$

where $\vartheta_N \equiv 1 - (-1)^N$ gives 0 for even N and 2 for odd N . Overall, the low-energy spectrum of a thin film has the form

$$E_{n \ll N|N}^{s,\tau}(\mathbf{k}) = \frac{\hbar^2}{2m_{c,z}} \frac{\pi^2 n^2}{d^2[N + 2v_0 + s\tau v_1 \vartheta_N]^2} + \frac{\hbar^2}{2m_{c,x|N}^{s,\tau}} (k_x - \kappa_{n|N}^{s,\tau})^2 + \frac{\hbar^2 k_y^2}{2m_{c,y|N}^{s,\tau}} + E_Q^0, \quad (28)$$

where the subband in-plane effective masses in the $\alpha = x, y$ directions are

$$[m_{\alpha,n|N}^{s,\tau}]^{-1} \approx m_{c,\alpha}^{-1} \left[1 + \frac{\zeta_\alpha \pi^2 n^2}{d^2[N + 2v_0 + s\tau v_1 \vartheta_N]^2} \right], \quad (29a)$$

and the momentum offset from the Q point is given by

$$\kappa_{n|N}^{s,\tau} \approx \tau \kappa_0 + \frac{\tau n^2 \pi^2 \beta}{d^2[N + 2v_0 + s\tau v_1 \vartheta_N]^2}. \quad (29b)$$

As in the monolayer case, the low-energy subband dispersions described by Eq. (28) near the six valleys at BZ points $\tau\mathbf{Q}$, $\tau C_3\mathbf{Q}$, and $\tau C_3^2\mathbf{Q}$, can be divided into two triads related by time-reversal symmetry, with quantum numbers $\tau = \pm 1$. The three valleys for a given τ are connected by C_3 rotations, as sketched in the inset of Fig. 2. As a consequence, for odd number of layers, where inversion symmetry is broken and SO splitting is parametrized by v_1 , the spin and valley degrees of freedom of the bottom subband are locked, and the low-energy states have valley degeneracy of $g_{\text{odd}} = 6$. Conversely, for even number of layers the bottom subbands are spin degenerate, giving a total degeneracy of $g_{\text{even}} = 12$. These large subband degeneracies and multivalley structures, together with the anisotropic dispersions found within each valley, may have important implications for the transport and quantum Hall properties of n -doped multilayer TMDs [48].

Both inversion and σ_h symmetry are broken when an electric field is applied along the \hat{z} axis of the film, leading to a modulation of the spin splittings in the case of odd N , and lifting of the spin degeneracy for even N . As a first approximation, this effect can be introduced into the lowest subband dispersion by substituting

$$E_Q^0 \rightarrow E_Q^0(\rho_e) + s\tau \Lambda(\rho_e) \quad (30)$$

in Eq. (28) for $n = 1$, where $\rho_e = 3 \sum_{s,\tau,n} \rho_n^{s\tau}$ is the total electron density induced by the field. These spin-dependent shifts of the band edges, abbreviated $E_{1|N}^s \equiv E_{1|N}^{s+}(\kappa_{1|N}^{s+}, 0)$, parametrize the symmetry breaking by the potential profile. As an example, representative of all four TMDs, Fig. 11 shows this splitting for the lowest conduction subband of five- and six-layer WSe₂, in the case where the field is induced by a single positive back gate near layer one. The corresponding induced electron densities and potential profiles were determined self-consistently to satisfy Eq. (22), and chosen inside a range that is easily accessible to experiments.

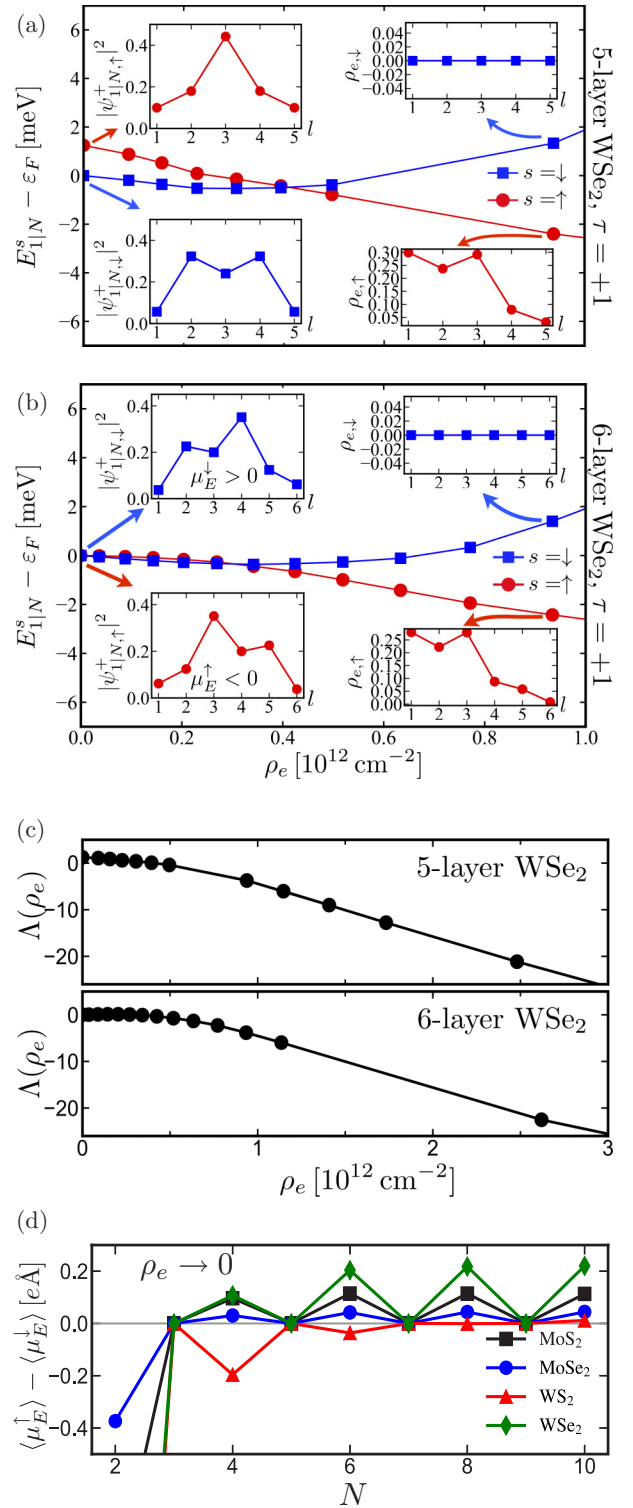


FIG. 11. Spin-up and -down subband edge energies $E_{1|N}^s$ at valley $\tau = +$, measured with respect to the Fermi level, for (a) five-layer and (b) six-layer WSe₂, as a function of electron density ρ_e . The potential profiles across the TMD film were determined self-consistently for a temperature of $T = 10$ K for a single (positive) back gate. In both panels, left and right insets show the spin-up and -down charge distributions for $\rho_e \rightarrow 0$ and for finite ρ_e , respectively. (c) Corresponding gate-doping-induced spin splittings at valley $\tau = +$. (d) Imbalance between the \hat{z} -axis electric dipole moments of the spin-up and -down subband edges for $\rho_e \rightarrow 0$.

In the case of even N , we can interpret the spin-splitting strength in the weak doping regime in terms of the spatial charge distributions of the lowest-energy spin-up and -down subband states. The left insets in Fig. 11(b) show the spread of these two states along the film's \hat{z} axis in the zero-doping limit ($\rho_e \rightarrow 0$). The two distributions are asymmetric with respect to the middle of the film, and related to each other by a $z \rightarrow -z$ mirror operation, resulting in opposite electric dipole moments $\langle \mu_E^\uparrow \rangle = -\langle \mu_E^\downarrow \rangle$ about the middle plane of the multilayer structure. The splitting in the zero-doping limit can be approximated as $\Lambda(\rho_e \rightarrow 0) \approx -(\langle \mu_E^\uparrow \rangle - \langle \mu_E^\downarrow \rangle)E_z > 0$, where $E_z > 0$ is the electric field in the \hat{z} direction. This is shown in Fig. 11(b) for electron densities between 0 and $0.2 \times 10^{12} \text{ cm}^{-2}$. This linear splitting contribution is weak: even at small doping, it is overcome by nonlinear screening effects, which produce a large negative splitting $\Lambda < 0$ [Fig. 11(c)] and quickly deplete the spin-down subband, as shown in the right insets of Fig. 11(b). For odd N , where in the zero-doping limit the states of both spin band edges are symmetric about the middle layer of the film [see insets of Fig. 11(a)], spin splitting is determined entirely by nonlinear effects. This analysis for the $\rho_e \rightarrow 0$ limit can be generalized to all even and odd values of N for all four TMDs, as shown in Fig. 11(d), where we show that, in all four cases, the spin-resolved electric dipole moments alternate between finite and zero for even and odd N , respectively. Also, note that according to Eq. (30), the sign of the spin splitting is inverted for opposite valleys.

B. Intersubband transitions and dispersion-induced line broadening in n -doped N -layer TMDs

Numerically diagonalizing the HkpTB Hamiltonian in Eq. (20) with the parameters of Tables IV and V, we obtain the energy spacings between the first and next few subbands of TMD films shown in Fig. 12. Using Eq. (28), we estimate the separation between the lowest two subbands of a given spin projection s as

$$E_{2|N}^{s,\tau} - E_{1|N}^{s,\tau} \approx \frac{15\pi^4 \hbar^2 \beta^2}{2m_{c,x} d^4 (N + 2\nu_0)^4} + \frac{3\pi^2 \hbar^2}{2m_{c,z} d^2 (N + 2\nu_0)^2} - \vartheta_N s \tau \nu_1 \frac{6\pi^2 \hbar^2}{2m_{c,z} d^2 (N + 2\nu_0)^3}. \quad (31)$$

Similarly, we estimate the splitting between the lowest subbands of opposite spin as

$$E_{1|N}^{-s,\tau} - E_{1|N}^{s,\tau} \approx s \tau \nu_1 \vartheta_N \frac{2\pi^2 \hbar^2}{2m_{c,z} d^2 (N + 2\nu_0)^3}. \quad (32)$$

We used Eqs. (31) and (32) to determine the boundary parameters ν_0 and ν_1 for each of the considered TMDs (MoS₂: $\nu_0 = 0.82, \nu_1 = -0.016$, MoSe₂: $\nu_0 = 0.76, \nu_1 = -0.0055$, WS₂: $\nu_0 = 0.80, \nu_1 = -0.0031$, WSe₂: $\nu_0 = 0.72, \nu_1 = -0.028$). The results are shown with solid lines in Fig. 12. In the absence of an electric field, the energy splitting between the lowest two spin-polarized transitions is of order few meV for the four TMDs. However, this splitting is enhanced by electron doping, as shown in Fig. 12(b) for two- to six-layer films of

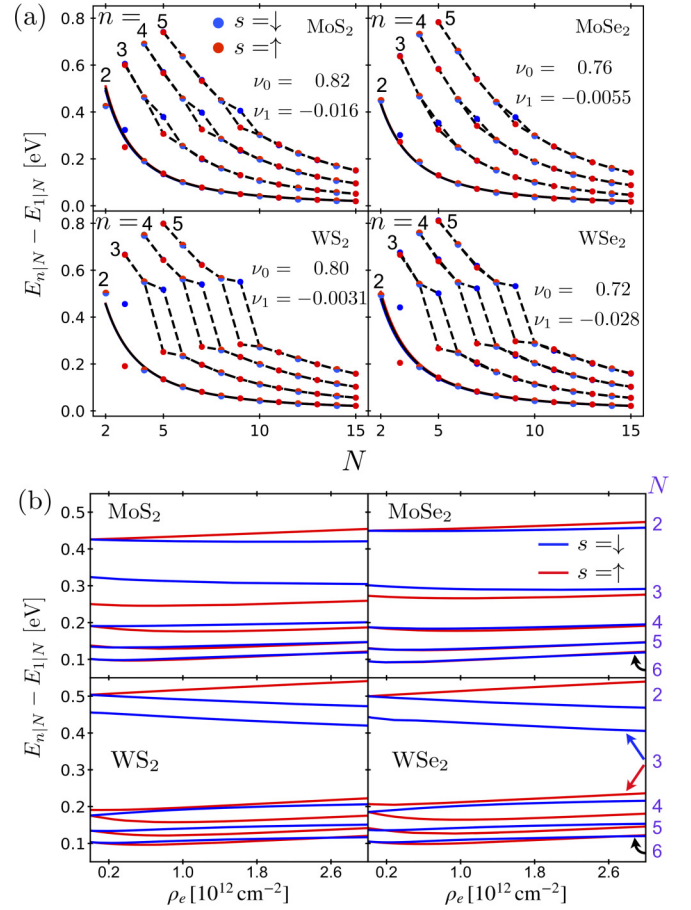


FIG. 12. (a) Energy spacings between the first and n th conduction subbands ($n = 2$ to 5) for the four TMDs, as functions of the number of layers N . The solid lines in each panel correspond to Eq. (31) for the main transition between the first and second subbands using the DFT bulk parameters, showing good agreement between the HkpTB model and DFT. Parameters ν_0 and ν_1 , fitted for $N \geq 4$, are given for the four TMDs in their corresponding panels. Blue (red) points and solid lines in each panel represent spin-down (-up) polarized subband spacings and fittings. Black points and solid line correspond to subband spacings for even N layers, where subbands are spin degenerate. (b) Lowest spin-up and -down subband transition as a function of total electron doping, for film thicknesses $N = 2$ to 6 layers. The number of layers N corresponding to each pair of curves is indicated on the right. For two layers, the doping level shifts the spin-up (spin-down) transition energy upward (downward) in energy, following a linear trend for moderate doping levels. For $N > 2$, nonlinear effects begin to appear already for weak doping, and the splitting of the spin-up and -down transitions is inverted with respect to $N = 2$.

all four TMDs. For $N = 2$, the spin-up (spin-down) transition energy grows (decreases) linearly with the doping level for small electron densities. The opposite trend is found for $N = 3$ to 6 , where the spin-up subband transition appears at lower energy, and nonlinear effects begin to appear already for low electron doping. We conclude that the electron doping level can be used as an additional tunable parameter to modify the energies and degeneracies of the lowest optical transitions in 2H-TMDs.

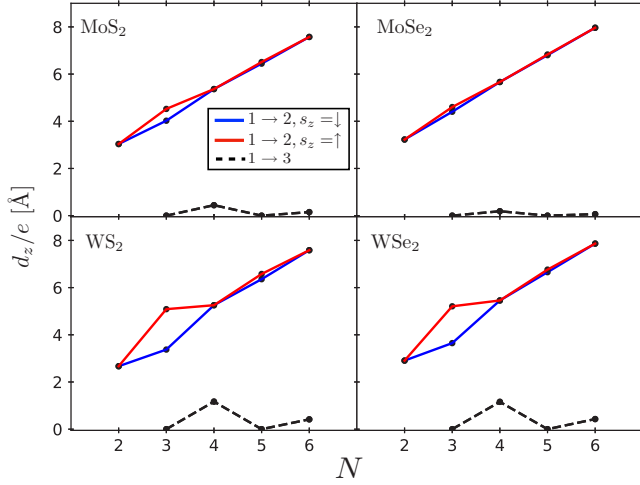


FIG. 13. Out-of-plane dipole moment matrix elements for the first two conduction intersubband transitions $1 \rightarrow 2$ (solid line) and $1 \rightarrow 3$ (dashed line). Transitions between spin-down (spin-up) subbands are shown in blue (red).

Next, we use the model developed above for electron subbands to study intersubband optical transitions, intersubband electron-phonon relaxation, and the intersubband absorption line shapes for IR/FIR light. As discussed in Sec. III B, the optical transition amplitude between two given subbands n, n' is determined by the out-of-plane dipole moment

$$d_{\tau, s; z}^{n, n'}(\mathbf{k}) = e \langle n, s; \tau, \mathbf{k} | z | n', s; \tau, \mathbf{k} \rangle$$

$$= e \sum_{j=1}^N z_j C_{n, j}^{\tau, s*}(\mathbf{k}) C_{n', j}^{\tau, s}(\mathbf{k}), \quad (33)$$

where N is the total number of layers, z_j denotes the z coordinate of layer j , and $C_{n, j}^{\tau, s}(\mathbf{k})$ are the components of the n th subband eigenstate of spin projection s and valley quantum number τ . The calculated dipole moment matrix element as a function of number of layers for the first two intersubband transitions is plotted in Fig. 13.

Similarly to the valence subband case, optical transitions in films with odd number of layers N are allowed only between states with opposite-parity subband indices, corresponding to opposite parity under σ_h transformation. The spin-orbit splitting present for odd N results in a spin selection rule, allowing transitions only between subbands with the same out-of-plane spin projection s . For even N , where σ_h symmetry is absent, transitions between subbands with same-parity indices are allowed. This is in contrast to the VB at the Γ point, and is a consequence of the multiple-valley structure of the CB, which makes it possible to form degenerate even and odd (under inversion) combinations of states, giving a finite dipole moment, as shown in Fig. 13 for the first two intersubband transitions, considering both spin-down and -up polarized subbands. This makes $1|N \rightarrow 2|N$ transition the dominant feature in the IR/FIR absorption by thin n -doped TMD films.

Similarly to the holes in p -doped TMDs, the line shape of the electron intersubband absorption in n -doped films is also affected by the difference between the effective masses of subbands $1|N$ and $2|N$. However, in contrast to the case of

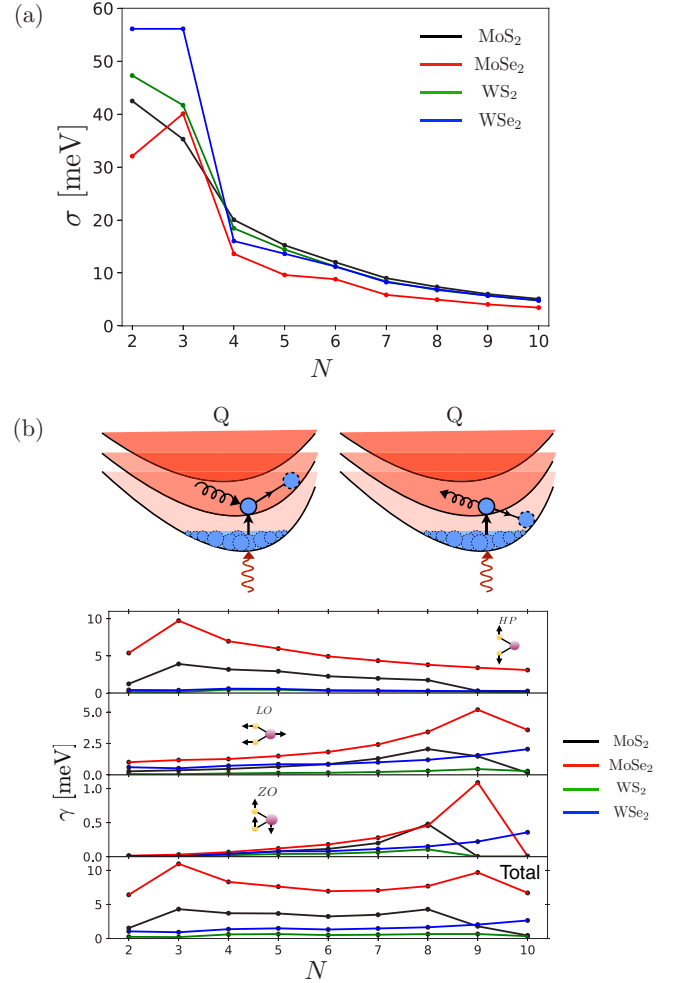


FIG. 14. (a) Absorption line widths for CB subbands at room temperature ($T = 300$ K) as a function of number of layers for the four TMDs, considering only DOS broadening. (b) Phonon-induced broadening at room temperature ($T = 300$ K) due to intersubband emission and intrasubband absorption of optical phonons in modes (top to bottom) HP, LO, and ZO. Results are shown for the four TMDs as a function of number of layers N , with the total broadening shown in the bottom panel.

holes, for electrons the line shapes depend also on the relative in-plane wave vectors of the conduction subband minima, as well as the anisotropic subband dispersions. The resulting broadening for N -layer $2H-MX_2$ films at room temperature, obtained numerically from the calculated line shapes, is shown in Fig. 14(a). Our calculations show that the aforementioned DOS broadening factors result in a typically larger broadening, which spreads the absorption spectrum towards both lower and higher energies from the main transition.

C. Electron-phonon relaxation and room-temperature absorption spectra in n -doped TMD films

The phonon-induced broadening for conduction subbands m and n , generated by intrasubband and intersubband

relaxation, is accounted for by

$$\gamma_{n,m}^{\tau,s} = 2\pi \sum_{\mu,\mathbf{q},j} \left| \sum_i g_{\mu}^{j,i}(\mathbf{q}) C_{n,i}^{\tau,s*}(\kappa_m^{\tau,s} \hat{x} + \mathbf{q}) C_{m,i}^{\tau,s}(\kappa_m^{\tau,s} \hat{x}) \right|^2 \times \{ [1 + n_T(\hbar\omega_{\mu})] \delta [E_m(\kappa_m^{\tau,s} \hat{x}) - E_n(\kappa_m^{\tau,s} \hat{x} + \mathbf{q}) - \hbar\omega_{\mu}] + \delta_{nm} n_T(\hbar\omega_{\mu}) \delta [E_m(\kappa_m^{\tau,s} \hat{x}) - E_m(\kappa_m^{\tau,s} \hat{x} + \mathbf{q}) + \hbar\omega_{\mu}] \}, \quad (34)$$

where $\kappa_m^{\tau,s}$ is the subband edge offset from the Q point of subband m with spin projection s , and $g_{\mu}^{j,i}$ are the electron-phonon couplings for the three phonon modes $\mu = \text{HP, LO, and ZO}$ given in Eq. (16), with D_v replaced by D_c for the HP phonon. The first term in Eq. (34) describes intersubband relaxation due to phonon emission, whereas the second describes intrasubband phonon absorption in the excited subband. The phonon-induced broadening for the four TMDs obtained using the electron-phonon coupling parameters in Table III are shown in Fig. 14(b). The dominant contribution comes from intersubband relaxation due to HP and LO phonon modes, with a smaller contribution from the thermally suppressed intrasubband absorption. The large HP phonon deformation potential at the Q point, as compared to its value at the Γ point [45], in particular for MoS_2 and MoSe_2 (see Table III), results in a large contribution to the broadening. Additional differences between the phonon-induced broadenings for the conduction and valence subbands originate from the different intersubband spacings as a function of number of layers (Figs. 5 and 12), and different dispersions (Figs. 4 and 10). As in the valence subbands case, the phonon broadening is most significant for MoSe_2 due to stronger electron-phonon coupling.

The absorption spectra of n -doped TMD films calculated using Fermi's golden rule, as in Eq. (18), and taking the discussions of Secs. IV A, IV B, and IV C into account, are shown in Fig. 15 for $N = 2$ to 5 layers. The predicted absorption spectra for the four TMDs are seen to be more symmetric than those for

the holes, primarily due to the effect of different dispersions in consecutive subbands, here aggravated by the shifts $\kappa_{n|N}^{\tau,s}$ and the BZ position of the subbands minima, in addition to the difference between the in-plane subband effective masses. The large SO splitting between the middle two subbands for $N = 3$ results in two distinct lines, whereas for $N = 5$ the spin-polarized subbands are nearly degenerate, resulting in the overlap of the two lines and giving a combined line with twice the amplitude.

V. CONCLUSIONS

We have presented hybrid $k \cdot p$ tight-binding models for the conduction and valence band edges of multilayer TMDs, capable of reproducing the rich low-energy subband dispersions, and allowing us to describe the intersubband optical transitions when coupled to out-of-plane polarized light. In particular, we find the following:

(i) The subbands at the CB edge are found near the Q valleys of the Brillouin zone, whereas the valence band edge is found at the Γ point. The main differences between the two sets of subbands are due to the significant spin-orbit splitting, multivalley structure, and anisotropic dispersions of the conduction subbands, by contrast to the valence subbands. These differences manifest themselves in the absorption line shapes and additional selection rules, particularly for odd number of layers, where spin-orbit splitting is present.

(ii) The four studied TMDs were found to have main intersubband transition energies for the conduction and valence subbands, which densely cover the spectrum range of wavelengths from $\lambda = 2 \mu\text{m}$ to $30 \mu\text{m}$ ($\hbar\omega = 40$ to 700 meV), for $N = 2$ to 7 layers. This allows tailoring structures of a specific material, appropriate type of doping, and number of layers for a particular device application, from IR to the THz range.

(iii) Two contributions to the absorption line-shape broadening are identified. The first, broadening due to intersubband phonon relaxation, is found to produce a meV limit to the intersubband linewidth. This is in contrast to III-V quantum wells, where phonon broadening is found to be more damaging to the intersubband transition line quality factor [30]. A second, elastic contribution to the line broadening caused by the different 2D masses of carriers in consecutive subbands yields a thermal broadening of the order of $k_B T$. Similarly to inhomogeneous broadening, this effect can be reduced by coupling the transition in the film to a standing wave of light in a high- Q resonator.

Finally, we propose a specific design of van der Waals multilayer structure utilizing the intersubband transitions in atomically thin films of TMDs. The sketch in Fig. 16 depicts the band configuration of a few-layer transition-metal dichalcogenide film, encapsulated by hexagonal boron nitride ($h\text{BN}$) and placed between two graphene electrodes. Applying a bias (and possibly also gate) voltage between the two electrodes results in a shift of the Dirac points relative to each other, and allows for the alignment of the Dirac point of the "top" graphene electrode with the lower-energy subband in the TMD, while keeping the Fermi level in graphene above the higher-energy subband. The carriers can then tunnel from the graphene electrode into the higher-energy subband. Once in the excited subband state, the carrier can undergo an intersubband transition, emitting light

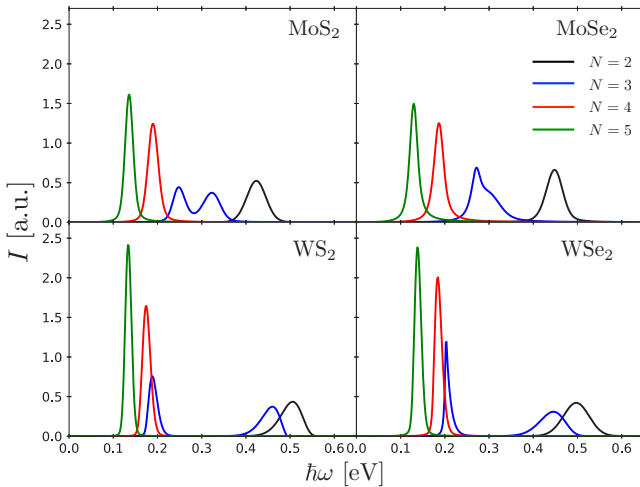


FIG. 15. Optical absorption lines for $N = 2$ –5 layers of lightly n -doped MoS_2 , MoSe_2 , WS_2 , and WSe_2 , taking into account intrinsic broadening at room temperature ($T = 300$ K). In the case of odd N , lines corresponding to different subband spin projections are summed.

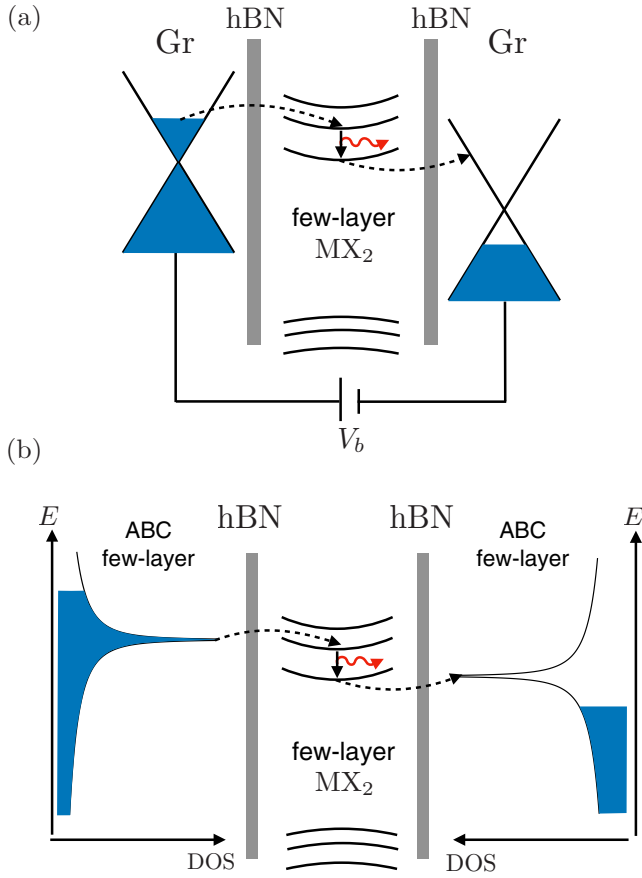


FIG. 16. Proposed device application for intersubband transitions in few-layer TMDs. (a) Few-layer TMDs encapsulated between two hexagonal boron nitride (hBN) crystals and two graphene (G) electrodes with an applied bias voltage between them. The applied bias voltage allows to realize light emission through intersubband transitions in the few-layer TMD system, by carriers tunneling between the two graphene electrodes. (b) An alternative realization using few-layer ABC-stacked graphene instead of monolayer, utilizing the Van Hove singularity in the density of states. The bias voltage aligns the Van Hove singularities near the second and first subbands, making the desired emission process more favorable.

polarized in the out-of-plane direction, followed by tunneling to the second graphene electrode from the bottom subband state.

A potentially more favorable realization of the above process which avoids carrier loss directly from the second subband, or carrier tunneling into the bottom subband, involves using ABC-stacked few-layer graphene. The band structure of ABC few-layer graphene has a Van Hove singularity in its density of states at the edge between conduction and valence bands. Aligning the Van Hove singularities of two such electrodes with the second and first subbands, respectively, would enable one to achieve preferential injection and extraction of carriers into/from the TMD film, thus offering a new way to produce functional optical fiber cables.

The proposed “LEGO”-type design of IR/THz emitting materials has potential for implementation as part of a composite optical fiber, where the coupling to the out-of-plane polarized photon would be supported by the waveguide mode.

ACKNOWLEDGMENTS

The authors acknowledge funding by the European Union’s Graphene Flagship Project, ERC Synergy Grant Hetero2D, EPSRC Doctoral Training Centre, Graphene NOWNANO, and the Lloyd Register Foundation Nanotechnology grant, as well as support from the N8 Polaris service and the use of the ARCHER supercomputer (RAP Project No. e547) and the Tianhe-2 supercomputer (Guangzhou, China). The authors would like to thank F. Koppens, K. Novoselov, R. Gorbachev, M. Potemski, R. Curry, C. Kocabas, S. Magorrian and A. Ceferino for fruitful discussions.

APPENDIX A: SYMMETRY CONSTRAINTS FOR THE BILAYER HAMILTONIANS

For $N = 2$ (bilayer), the Hamiltonian must be invariant under spatial inversion \mathcal{P} , $x \rightarrow -x$ mirror symmetry $\mathcal{D}(\sigma_v)$, and time reversal \mathcal{T} . For the conduction band model about the Q point, this gives the conditions [49]

$$\mathcal{P}H_2^\tau(\mathbf{k})\mathcal{P}^{-1} = H_2^{-\tau}(-\mathbf{k}), \quad (\text{A1a})$$

$$\mathcal{D}(\sigma_v)H_2^\tau(k_x, k_y)\mathcal{D}^{-1}(\sigma_v) = H_2^{-\tau}(-k_x, k_y), \quad (\text{A1b})$$

$$\mathcal{T}H_2^\tau(\mathbf{k})\mathcal{T}^{-1} = H_2^{-\tau}(-\mathbf{k}). \quad (\text{A1c})$$

We have $\mathcal{P} = \pi_1 s_0$, $\mathcal{D}(\sigma_v) = \pi_0 s_1$, and $\mathcal{T}_2 = -i\pi_0 s_2 \mathcal{C}$, where π_j (s_j) are Pauli matrices acting on the layer (spin) subspace, and \mathcal{C} represents complex conjugation. As a result, the most general valley-spin structure for the bilayer Hamiltonian at the τQ valley is

$$H_2^\tau(\mathbf{k}) = \sum_{i,j=0}^3 A_{ij}^\tau(\mathbf{k})\pi_i s_j, \quad (\text{A2})$$

where the symmetry constraints (A1a)–(A1c) require that

$$A_{i0}^\tau(k_x, k_y) = A_{i0}^{-\tau}(-k_x, k_y) = A_{i0}^\tau(k_x, -k_y), \quad i = 0, 1 \quad (\text{A3a})$$

$$A_{20}^\tau(k_x, k_y) = A_{20}^{-\tau}(-k_x, k_y) = -A_{20}^\tau(k_x, -k_y), \quad (\text{A3b})$$

$$A_{31}^\tau(k_x, k_y) = A_{31}^{-\tau}(-k_x, k_y) = -A_{31}^\tau(k_x, -k_y), \quad (\text{A3c})$$

$$A_{32}^\tau(k_x, k_y) = -A_{32}^{-\tau}(-k_x, k_y) = A_{32}^\tau(k_x, -k_y), \quad (\text{A3d})$$

$$A_{33}^\tau(k_x, k_y) = -A_{33}^{-\tau}(-k_x, k_y) = A_{33}^\tau(k_x, -k_y). \quad (\text{A3e})$$

One can check that, for $N = 2$, Eq. (20) corresponds to $A_{00}^\tau(\mathbf{k}) = \frac{E_1^+(\mathbf{k}) + E_2^+(\mathbf{k})}{2}$, $A_{33}^\tau(\mathbf{k}) = \tau \frac{E_1^+(\mathbf{k}) - E_2^+(\mathbf{k})}{2}$, $A_{10}^\tau(\mathbf{k}) = t_0 + \tau t_1 k_x + t_2 k_x^2 + u_2 k_y^2$, and $A_{20}^\tau(\mathbf{k}) = -u_1 k_y$, and that these terms meet the symmetry requirements. Furthermore, we carried out fittings to DFT data using the additional spin-orbit terms $A_{32}^\tau(\mathbf{k}) = \alpha k_x$ and $A_{31}^\tau(\mathbf{k}) = \beta k_y$. The fittings give $|\alpha|, |\beta|, |u_1| \ll |t_1|$; hence, we conclude that these terms can be neglected.

For the interlayer hopping used in the HkpTB model for the valence band near Γ , setting $N = 2$ in Eq. (3) and using a basis ordering similar to that of Eq. (5), we have $\mathcal{T} = \pi_0 \sigma_0 \mathcal{C}$, $\mathcal{P} = \pi_1 \sigma_3$, and $\mathcal{D}(\sigma_v) = \pi_0 \sigma_0$, where σ_i act on the band (v and w) subspace. The symmetry conditions require

$$\text{Re } t_\sigma(\mathbf{k}) = \text{Re } t_\sigma(-\mathbf{k}) = \text{Re } t_\sigma(-k_x, k_y), \quad (\text{A4a})$$

$$\text{Im } t_\sigma(\mathbf{k}) = -\text{Im } t_\sigma(-\mathbf{k}) = \text{Im } t_\sigma(-k_x, k_y), \quad (\text{A4b})$$

$$t_{vw}(\mathbf{k}) = t_{vw}(-\mathbf{k}) = t_{vw}(-k_x, k_y), \quad t_{vw} \in \mathbb{R}. \quad (\text{A4c})$$

APPENDIX B: SPIN-ORBIT-COUPLING-INDUCED INTERBAND COUPLING AT THE Γ -POINT VALENCE BANDS

Here, we analyze the role of spin-orbit coupling and coupling to distant bands in determining parameters for the valence band HkpTB model. The spin-orbit coupling is given by $\hat{H}_{\text{SO}} = \lambda \hat{\mathbf{L}} \cdot \hat{\mathbf{S}}$, where $\hat{\mathbf{L}}$ and $\hat{\mathbf{S}}$ are the orbital and spin angular momentum operators. This can also be written in terms of the ladder operators $L_{\pm} = L_x \pm iL_y$ and $S_{\pm} = (S_x \pm iS_y)/2$ as

$$\hat{H}_{\text{SO}} = \lambda(L_z S_z + L_+ S_- + L_- S_+), \quad (\text{B1})$$

where $L_{\pm} S_{\mp}$ describe a spin flip with corresponding change in orbital angular momentum projection. These terms couple the v and w bands with the bands v_1 and v_3 [Fig. 2(d)], which in the absence of SO coupling are doubly degenerate. Band v_1 (E'' Irrep of C_{3d}) has basis functions which are odd under $z \rightarrow -z$ (metal $d_{\pm 1}$ orbitals being the dominant component [27], as well as chalcogen $p_{\pm 1}$). Band v_3 (E' Irrep of C_{3d}) has basis functions even under $z \rightarrow -z$ (metal $d_{\pm 2}$ orbitals and chalcogen $p_{\pm 1}$). Including SO coupling results in the splitting of these bands into new bands denoted by the orbital and spin angular momentum projections along \hat{z} , $v_1(\pm 3/2), v_3(\pm 3/2)$, and $v_1(\pm 1/2), v_3(\pm 1/2)$, corresponding to total angular momentum projections of $J_z = \pm 3/2$ and $J_z = \pm 1/2$, respectively.

The v band belongs to the one-dimensional A_1' Irrep (even under $z \rightarrow -z$, with metal d_0 dominant and chalcogen p_0), and has $L_z = 0$ and $s_z = \pm 1/2$. Similarly, the w band belongs to the one-dimensional A_2' Irrep, and is dominated by the odd (under $z \rightarrow -z$) chalcogen p_0 orbitals, giving two states with $L_z = 0$ and $s_z = \pm 1/2$.

Therefore, in the bilayer, where $z \rightarrow -z$ symmetry is broken, the v and w bands can couple to v_1 and v_3 bands, with the

appropriate spin-flip terms. In the second-order perturbation theory, this coupling produces corrections to the onsite energy

$$\delta_{\sigma} = \sum_{\substack{L_z, s_z \\ i=1,3 \\ \sigma=v,w}} \frac{|\langle v_i(L_z, s_z) | \lambda L_{\pm} S_{\mp} | \sigma(L_z = 0, s_z = \pm 1/2) \rangle|^2}{E_{\sigma} - E_{v_i(L_z, s_z)}}. \quad (\text{B2})$$

Note that these corrections are the same for both spin components of the v or w bands, with only one of the terms $L_{\pm} S_{\mp}$ contributing for a given spin state.

An additional SO-induced interband coupling with a spin flip may be present in the multilayer case, affecting the interlayer coupling

$$\hat{H}'_{\text{SO}} = \mu \hat{z} \cdot (\mathbf{k} \times \mathbf{S}) = i\mu(S_- k_+ - S_+ k_-), \quad (\text{B3})$$

where the prefactor μ is related to the gradient of the interlayer pseudopotential $\mu \propto \partial_z V$, and we defined $k_{\pm} = k_x \pm ik_y$. In contrast to the previous coupling, this coupling has a k dependence, which affects the dispersions. The coupling in Eq. (B3) is odd under spatial inversion. Due to the 2H-stacked bilayer having spatial inversion symmetry, the coupling is nonzero only between different bands in the two layers. In second-order perturbation theory, we get a nominal redefinition of the 2D mass used in the HkpTB model, by adding the term

$$\mu_{\sigma}(\mathbf{k}) = \sum_{v_i} \frac{|\langle v_i | \mu S_{\mp} k_{\pm} | \sigma \rangle|^2}{E_{\sigma} - E_{v_i}} = \mu_{\sigma} k^2, \quad (\text{B4})$$

with μ_{σ} a fitting parameter.

APPENDIX C: SPIN-SPLIT BANDS AT THE BRILLOUIN ZONE EDGE FOR ODD NUMBER OF LAYERS

The effective Q -point Hamiltonians $H_{NQ}^{\tau}(\mathbf{k})$ for N odd can be split into two decoupled blocks of different spin projection as $H_{NQ}^{\tau}(\mathbf{k}) = \text{diag}\{h_N^{\tau, \uparrow}(\mathbf{k}), h_N^{\tau, \downarrow}(\mathbf{k})\}$, where the blocks have the alternating $N \times N$ matrix form

$$h_N^{\tau, s}(\mathbf{k}) = \begin{pmatrix} \varepsilon_0(\mathbf{k}) + s\tau\Delta(\mathbf{k}) & t_{\tau}(\mathbf{k}) & 0 & 0 & \dots & 0 \\ t_{\tau}^*(\mathbf{k}) & \varepsilon_0(\mathbf{k}) - s\tau\Delta(\mathbf{k}) & t_{\tau}^*(\mathbf{k}) & 0 & \dots & 0 \\ 0 & t_{\tau}(\mathbf{k}) & \varepsilon_0(\mathbf{k}) + s\tau\Delta(\mathbf{k}) & t_{\tau}(\mathbf{k}) & \dots & 0 \\ 0 & 0 & t_{\tau}^*(\mathbf{k}) & \varepsilon_0(\mathbf{k}) - s\tau\Delta(\mathbf{k}) & \dots & 0 \\ \vdots & \vdots & \vdots & \vdots & \ddots & t_{\tau}(\mathbf{k}) \\ 0 & 0 & 0 & \dots & t_{\tau}^*(\mathbf{k}) & \varepsilon_0(\mathbf{k}) + s\tau\Delta(\mathbf{k}) \end{pmatrix}, \quad (\text{C1})$$

and we have defined

$$\varepsilon_0(\mathbf{k}) = \frac{E_{\uparrow}^+(\mathbf{k}) + E_{\downarrow}^+(\mathbf{k})}{2}, \quad (\text{C2a})$$

$$\Delta(\mathbf{k}) = \frac{E_{\uparrow}^+(\mathbf{k}) - E_{\downarrow}^+(\mathbf{k})}{2}. \quad (\text{C2b})$$

Defining the even-dimensional $(N - 1) \times (N - 1)$ matrix

$$\tilde{h}_{N-1}^{\tau,s}(\mathbf{k}) = \begin{pmatrix} \varepsilon_0(\mathbf{k}) - s\tau\Delta(\mathbf{k}) & t_\tau^*(\mathbf{k}) & 0 & \cdots & 0 \\ t_\tau(\mathbf{k}) & \varepsilon_0(\mathbf{k}) + s\tau\Delta(\mathbf{k}) & t_\tau(\mathbf{k}) & \cdots & 0 \\ 0 & t_\tau^*(\mathbf{k}) & \varepsilon_0(\mathbf{k}) - s\tau\Delta(\mathbf{k}) & \cdots & 0 \\ \vdots & \vdots & \vdots & \ddots & t_\tau(\mathbf{k}) \\ 0 & 0 & \cdots & t_\tau^*(\mathbf{k}) & \varepsilon_0(\mathbf{k}) + s\tau\Delta(\mathbf{k}) \end{pmatrix}, \quad (\text{C3})$$

the eigenvalues ε of (C1) are given by a secular equation

$$\begin{aligned} \det\{\varepsilon - h_N^{\tau,s}\} &= [\varepsilon - \varepsilon_0(\mathbf{k}) - s\tau\Delta(\mathbf{k})] \det\{\varepsilon - \tilde{h}_{N-1}^{\tau,s}\} - |t_\tau(\mathbf{k})|^2 \det\{\varepsilon - h_{N-2}^{\tau,s}\} \\ &= [\varepsilon - \varepsilon_0(\mathbf{k}) - s\tau\Delta(\mathbf{k})] \det\{\varepsilon - \tilde{h}_{N-1}^{\tau,s}\} - |t_\tau(\mathbf{k})|^2 ([\varepsilon - \varepsilon_0(\mathbf{k}) - s\tau\Delta(\mathbf{k})] \det\{\varepsilon - \tilde{h}_{N-3}^{\tau,s}\} \\ &\quad - |t_\tau(\mathbf{k})|^2 \det\{\varepsilon - h_{N-4}^{\tau,s}\}) = \cdots. \end{aligned} \quad (\text{C4})$$

Using the fact that $\det\{\varepsilon - h_1^{\tau,s}\} = \varepsilon - \varepsilon_0(\mathbf{k}) - s\tau\Delta(\mathbf{k})$, we can continue expanding Eq. (C4) to obtain

$$\det\{\varepsilon - h_N^{\tau,s}\} = [\varepsilon - \varepsilon_0(\mathbf{k}) - s\tau\Delta(\mathbf{k})] \left(\sum_{m=0}^{\frac{N-3}{2}} (-1)^m |t_\tau(\mathbf{k})|^{2m} \det\{\varepsilon - \tilde{h}_{N-(2m+1)}\} + (-1)^{\frac{N-1}{2}} |t_\tau(\mathbf{k})|^{N-1} \right), \quad (\text{C5})$$

which explicitly shows that $[\varepsilon - \varepsilon_0(\mathbf{k}) - s\tau\Delta(\mathbf{k})]$ is an overall factor, and thus $\varepsilon = \varepsilon_0(\mathbf{k}) + s\tau\Delta(\mathbf{k}) \equiv \varepsilon_s^\tau(\mathbf{k})$ is always an eigenvalue, regardless of the (odd) value of N . For a given τ , the different s quantum numbers give two spin-split monolayer dispersions $\varepsilon_s^\tau(\mathbf{k})$ about the $\tau C_3^m \mathbf{Q}$ ($m = 0, 1, 2$) points, corresponding to the features observed in Fig. 10. The fact that this prediction is verified in the DFT band structures clearly confirms the validity of our hybrid model.

For large odd N , nearly spin-degenerate bands grow denser on either side of the spin-split bands $\varepsilon_s^\tau(\mathbf{k})$ without crossing them, as shown in Fig. 17(a). The reason for this becomes clear when we take the bulk limit, and find that the spin-split states form the band edges around a central gap in the subband structure. This is shown in Fig. 17(b). Indeed, in the limit of large N the Hamiltonian (C1) corresponds to the bulk Hamiltonian at $k_z = \pi/c$ since $\varepsilon_0(\mathbf{k}) = \varepsilon_0(\mathbf{k}, k_z = \frac{\pi}{c})$ [see Eq. (23)].

APPENDIX D: ELECTRON-PHONON COUPLING FOR LO PHONON IN MULTILAYER SYSTEM

In this appendix, we derive the expression used for the electron-phonon coupling with LO phonon in a multilayer system. As described in the text, we treat the LO phonon in each layer as independent and degenerate. However, in the LO phonon case, the generated electrostatic potential due LO phonon in one layer interacts with the electrons in all the other layers in the system, following similar steps as in Ref. [50].

Within a monolayer, the LO phonon-induced in-plane polarization is given by its in-plane Fourier component

$$\mathbf{P}_q(z) = \frac{eZ}{\epsilon(q)A} \mathbf{u}_q \delta(z), \quad (\text{D1})$$

where Z is the Born effective charge on the metal and chalcogens, A is the unit-cell area, $\mathbf{u}_q = \sqrt{\frac{\hbar}{2M_r N_{\text{cell}} \omega_{\text{LO}}}} \hat{\mathbf{e}}$ is the phonon-induced atomic displacement in the direction connecting the metal and chalcogens in the unit cell, with M_r the reduced mass of the metal and chalcogens, N the number of unit cells in the sample, and ω_{LO} the LO phonon frequency. $\epsilon(q)$ is the dielectric function characterizing the response of the material to the phonon induced electric field.

The induced charge density in the layer is given by $\rho = -\nabla \cdot \mathbf{P}$, with the Fourier component

$$\rho_q = -i\mathbf{q} \cdot \mathbf{P}_q. \quad (\text{D2})$$

The potential resulting from the charge distribution is given by Poisson's equation $\nabla^2 \phi = -4\pi\rho$. Fourier transforming in

three dimensions gives

$$\phi_q(k) = \frac{-4\pi i e Z}{\epsilon(q)A} \frac{\mathbf{q} \cdot \mathbf{u}_q}{q^2 + k^2}, \quad (\text{D3})$$

where k is the Fourier parameter in the z direction. Inverse Fourier transforming in k gives the z dependence of the potential with in-plane Fourier component \mathbf{q} :

$$\phi_q(z) = -i \frac{2\pi e Z \mathbf{u}_q}{\epsilon(q)A} e^{-q|z|}. \quad (\text{D4})$$

The electron-phonon coupling for an electron localized in an isolated monolayer is given by $g(q) = e\phi_q(0) = -i \frac{2\pi e^2 Z \mathbf{u}_q}{\epsilon A}$. This form of the coupling is similar to the form derived in Refs. [28,43], where the polarizability of a two-dimensional dielectric was taken into account by the replacement $\epsilon(q) \rightarrow 1 + r_* q$, with r_* the screening length in the material. For multilayer 2H-stacked TMDs, as the polarization in subsequent layers alternates in its sign, the resulting electrostatic potential also alternates in its sign.

APPENDIX E: ELECTRON-PHONON COUPLING FOR ZO PHONON IN MULTILAYER SYSTEM

The atomic vibrations for the ZO optical phonon mode result in a polarization in the out-of-plane direction due to the opposite motions of the metal and two chalcogens, and the finite Born effective charges in the z direction. The interaction energy in the multilayer system between charges and phonon-

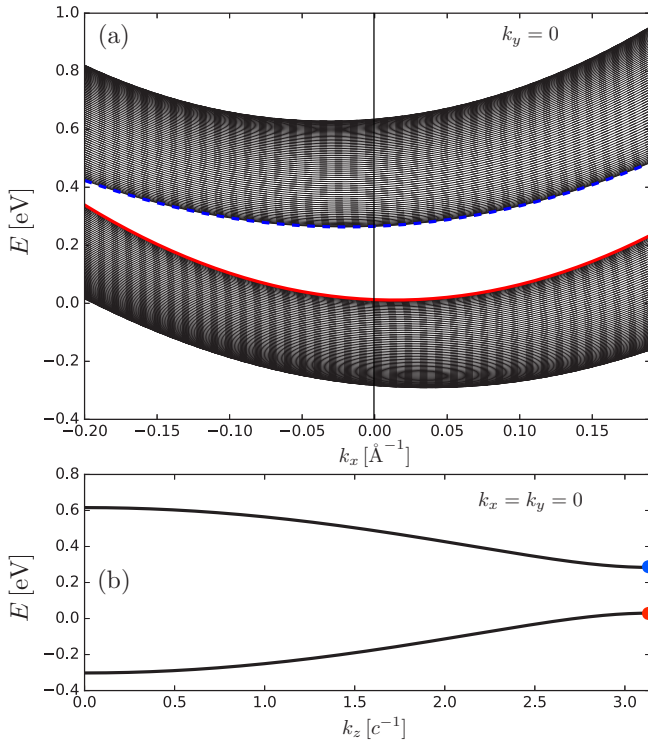


FIG. 17. (a) Subband structure of 101-layer WS_2 near $\tau\mathbf{Q}$ ($k_x = 0$), along the $\Gamma\bar{K}$ line. Spin-up (-down) bands are shown with solid (dashed) curves. The spin-split bands $\varepsilon_s^\pm(\mathbf{k})$, pinned in the middle of the odd N subband structure, are shown in blue and red. (b) Bulk band structure for WS_2 along the 3D BZ line indicated in the inset of Fig. 9. Blue and red dots mark the position of the spin-split bands in the Brillouin zone.

induced out-of-plane polarizations in all layers is given by [51]

$$E_{\text{int}} = \sum_{n,m} \int d^2r d^2r' \frac{\rho_n(\mathbf{r}) P_{z,m}(\mathbf{r}') d(n-m)}{\Delta r^3},$$

$$\Delta r = [(\mathbf{r} - \mathbf{r}')^2 + d^2(n-m)^2]^{1/2}, \quad (\text{E1})$$

where $\rho_n(\mathbf{r})$ is the charge density on layer n , $P_{z,m}(\mathbf{r}')$ is the out-of-plane polarization in layer m caused by the ZO optical phonon, d the interlayer separation, and we sum over all layer pairs. Fourier transforming the charge density and polarization in the in-plane momentum components gives

$$\rho_n(\mathbf{r}) = \int \frac{d^2q}{(2\pi)^2} e^{i\mathbf{q}\cdot\mathbf{r}} \rho_n(\mathbf{q}), \quad (\text{E2})$$

and similarly for the polarization. The interaction energy then takes the form

$$E_{\text{int}} = \sum_{n,m} \int d^2r d^2r' \frac{d(n-m)}{\Delta r^3} \times \int \frac{d^2q d^2q'}{(2\pi)^4} e^{i\mathbf{q}\cdot\mathbf{r}} e^{i\mathbf{q}'\cdot\mathbf{r}'} \rho_n(\mathbf{q}) P_{z,m}(\mathbf{q}'). \quad (\text{E3})$$

Defining the new variables $\tilde{\mathbf{r}} = \mathbf{r} - \mathbf{r}'$, $\mathbf{R} = \mathbf{r} + \mathbf{r}'$, and integrating over \mathbf{R} gives $\delta_{q,-q'}$,

$$E_{\text{e-ph}} = \sum_{n,m} \int d^2\tilde{r} \int \frac{d^2q}{(2\pi)^2} \frac{d(n-m)}{\Delta \tilde{r}^3} e^{i\mathbf{q}\cdot\tilde{\mathbf{r}}} \times \rho_n^*(\mathbf{q}) P_{z,m}(\mathbf{q}), \quad (\text{E4})$$

where in the last row we used $\rho_n^*(\mathbf{q}) = \rho_n(-\mathbf{q})$ since the density is real. Carrying out the integration over $\tilde{\mathbf{r}}$ gives

$$E_{\text{e-ph}} = \sum'_{n,m} \frac{2\pi(n-m)}{|n-m|} \int \frac{d^2q}{(2\pi)^2} e^{-qd|n-m|} \rho_n^*(\mathbf{q}) P_{z,m}(\mathbf{q}), \quad (\text{E5})$$

where the prime over the sum means that the summation excludes the term with $n = m$. Quantizing the phonon polarization and the carrier density gives

$$\rho_n^*(\mathbf{q}) = e \sum_{\mathbf{k}} c_{\mathbf{k},n}^\dagger c_{\mathbf{k}+\mathbf{q},n},$$

$$P_{z,m}(\mathbf{q}) = \frac{eZ_z}{A} \sqrt{\frac{\hbar}{2N_{\text{cell}}M_r\omega}} (a_{-\mathbf{q},m} + a_{\mathbf{q},m}^\dagger), \quad (\text{E6})$$

where $c_{\mathbf{k},n}$ ($c_{\mathbf{k},n}^\dagger$) is the annihilation (creation) operator for an electron in state \mathbf{k} in layer n , and $a_{\mathbf{q},m}$ ($a_{\mathbf{q},m}^\dagger$) is the annihilation (creation) operator for a phonon with in-plane wave vector \mathbf{q} . The phonon-induced polarization is given, similarly to the LO phonon case, by the Born effective charge and the phonon displacement.

The electron-phonon interaction Hamiltonian is then given by

$$H_{\text{e-ph}} = \frac{2\pi e^2 Z_z}{A} \sqrt{\frac{\hbar}{2N_{\text{cell}}M_r\omega_{\text{ZO}}}} \sum'_{n,m} \sum_{\mathbf{k},\mathbf{q}} \frac{n-m}{|n-m|} e^{-qd|n-m|} \times c_{\mathbf{k},n}^\dagger c_{\mathbf{k}+\mathbf{q},n} (a_{-\mathbf{q},m} + a_{\mathbf{q},m}^\dagger). \quad (\text{E7})$$

- [1] D. Jariwala, V. K. Sangwan, L. J. Lauhon, T. J. Marks, and M. C. Hersam, *ACS Nano* **8**, 1102 (2014).
 [2] W. Choi, N. Choudhary, G. H. Han, J. Park, D. Akinwande, and Y. H. Lee, *Mater. Today* **20**, 116 (2017).
 [3] Y. Zhao, W. Yu, and G. Ouyang, *J. Phys. D: Appl. Phys.* **51**, 015111 (2018).
 [4] Q. H. Wang, K. Kalantar-Zadeh, A. Kis, J. N. Coleman, and M. S. Strano, *Nat. Nanotechnol.* **7**, 699 (2012).

- [5] G.-B. Liu, D. Xiao, Y. Yao, X. Xu, and W. Yao, *Chem. Soc. Rev.* **44**, 2643 (2015).
 [6] K. F. Mak and J. Shan, *Nat. Photonics* **10**, 216 (2016).
 [7] U. Wurstbauer, B. Miller, E. Parzinger, and A. W. Holleitner, *J. Phys. D: Appl. Phys.* **50**, 173001 (2017).
 [8] K. F. Mak, C. Lee, J. Hone, J. Shan, and T. F. Heinz, *Phys. Rev. Lett.* **105**, 136805 (2010).

- [9] G. Aivazian, Z. Gong, A. M. Jones, R.-L. Chu, J. Yan, D. G. Mandrus, C. Zhang, D. Cobden, W. Yao, and X. Xu, *Nat. Phys.* **11**, 148 (2015).
- [10] D. MacNeill, C. Heikes, K. F. Mak, Z. Anderson, A. Kormányos, V. Zólyomi, J. Park, and D. C. Ralph, *Phys. Rev. Lett.* **114**, 037401 (2015).
- [11] B. Zhu, H. Zeng, J. Dai, and X. Cui, *Adv. Mater.* **26**, 5504 (2014).
- [12] L. Yang, N. A. Sinitsyn, W. Chen, J. Yuan, J. Zhang, J. Lou, and S. A. Crooker, *Nat. Phys.* **11**, 830 (2015).
- [13] H. Yu, G.-B. Liu, P. Gong, X. Xu, and W. Yao, *Nat. Commun.* **5**, 3876 (2014).
- [14] D. Gunlycke and F. Tseng, *Phys. Chem. Chem. Phys.* **18**, 8579 (2016).
- [15] T. Cheiwchanchamnangij and W. R. L. Lambrecht, *Phys. Rev. B* **85**, 205302 (2012).
- [16] E. Cappelluti, R. Roldán, J. A. Silva-Guillén, P. Ordejón, and F. Guinea, *Phys. Rev. B* **88**, 075409 (2013).
- [17] L. Debbichi, O. Eriksson, and S. Lebegue, *Phys. Rev. B* **89**, 205311 (2014).
- [18] J. E. Padilha, H. Peelaers, A. Janotti, and C. G. Van de Walle, *Phys. Rev. B* **90**, 205420 (2014).
- [19] T.-R. Chang, H. Lin, H.-T. Jeng, and A. Bansil, *Sci. Rep.* **4**, 6270 (2014).
- [20] S. Fang, R. Kuate Defo, S. N. Shirodkar, S. Lieu, G. A. Tritsarlis, and E. Kaxiras, *Phys. Rev. B* **92**, 205108 (2015).
- [21] A. J. Bradley, M. M. Ugeda, F. H. da Jornada, D. Y. Qiu, W. Ruan, Y. Zhang, S. Wickenburg, A. Riss, J. Lu, S.-K. Mo, Z. Hussain, Z.-X. Shen, S. G. Louie, and M. F. Crommie, *Nano Lett.* **15**, 2594 (2015).
- [22] Y. Sun, D. Wang, and Z. Shuai, *J. Phys. Chem. C* **120**, 21866 (2016).
- [23] R. Pisoni, Y. Lee, H. Overweg, M. Eich, P. Simonet, K. Watanabe, T. Taniguchi, R. Gorbachev, T. Ihn, and K. Ensslin, *Nano Lett.* **17**, 5008 (2017).
- [24] S. J. Magorrian, V. Zólyomi, and V. I. Fal'ko, *Phys. Rev. B* **94**, 245431 (2016).
- [25] D. A. Bandurin, A. V. Tyurnina, G. L. Yu, A. Mishchenko, V. Zólyomi, S. V. Morozov, R. K. Kumar, R. V. Gorbachev, Z. R. Kudrynskiy, S. Pezzini, Z. D. Kovalyuk, U. Zeitler, K. S. Novoselov, A. Patané, L. Eaves, I. V. Grigorieva, V. I. Fal'ko, A. K. Geim, and Y. Cao, *Nat. Nanotechnol.* **12**, 223 (2016).
- [26] A. Kormányos, V. Zólyomi, N. D. Drummond, P. Rakyta, G. Burkard, and V. I. Fal'ko, *Phys. Rev. B* **88**, 045416 (2013).
- [27] A. Kormányos, G. Burkard, M. Gmitra, J. Fabian, V. Zólyomi, N. D. Drummond, and V. Fal'ko, *2D Mater.* **2**, 022001 (2015).
- [28] M. Danovich, I. L. Aleiner, N. D. Drummond, and V. I. Fal'ko, *IEEE J. Sel. Top. Quantum Electron.* **23**, 168 (2017).
- [29] D. Kozawa, R. Kumar, A. Carvalho, K. Kumar Amara, W. Zhao, S. Wang, M. Toh, R. M. Ribeiro, A. H. Castro Neto, K. Matsuda, and G. Eda, *Nat. Commun.* **5**, 4543 (2014).
- [30] T. Unuma, M. Yoshita, T. Noda, H. Sakaki, and H. Akiyama, *J. Appl. Phys.* **93**, 1586 (2003).
- [31] L. F. Mattheiss, *Phys. Rev. B* **8**, 3719 (1973).
- [32] See Supplemental Material at <http://link.aps.org/supplemental/10.1103/PhysRevB.98.035411> for detailed DFT band structure results of 2H-stacked N -layer films ($N = 3$ to 6) of all four transition-metal dichalcogenides discussed in this paper, as well as fittings of our hybrid $k \cdot p$ tight-binding models to DFT data.
- [33] P. Giannozzi, S. Baroni, N. Bonini, M. Calandra, R. Car, C. Cavazzoni, D. Ceresoli, G. L. Chiarotti, M. Cococcioni, I. Dabo *et al.*, *J. Phys.: Condens. Matter* **21**, 395502 (2009).
- [34] J. P. Perdew and A. Zunger, *Phys. Rev. B* **23**, 5048 (1981).
- [35] A. Dal Corso, *Comput. Mater. Sci.* **95**, 337 (2014).
- [36] H. J. Monkhorst and J. D. Pack, *Phys. Rev. B* **13**, 5188 (1976).
- [37] M. Methfessel and A. T. Paxton, *Phys. Rev. B* **40**, 3616 (1989).
- [38] T. Böker, R. Severin, A. Müller, C. Janowitz, R. Manzke, D. Voß, P. Krüger, A. Mazur, and J. Pollmann, *Phys. Rev. B* **64**, 235305 (2001).
- [39] A. A. Al-Hilli and B. L. Evans, *J. Cryst. Growth* **15**, 93 (1972).
- [40] T. J. Wieting, *J. Phys. Chem. Solids* **31**, 2148 (1970).
- [41] W. T. Hicks, *J. Electrochem. Soc.* **111**, 1058 (1964).
- [42] S. J. Magorrian, A. Ceferino, V. Zólyomi, and V. I. Fal'ko, *Phys. Rev. B* **97**, 165304 (2018).
- [43] T. Sohler, M. Calandra, and F. Mauri, *Phys. Rev. B* **94**, 085415 (2016).
- [44] G. Froehlicher, E. Lorchat, F. Fernique, C. Joshi, A. Molina-Sánchez, L. Wirtz, and S. Berciaud, *Nano Lett.* **15**, 6481 (2015).
- [45] Z. Jin, X. Li, J. T. Mullen, and K. W. Kim, *Phys. Rev. B* **90**, 045422 (2014).
- [46] X. Gu and R. Yang, *Appl. Phys. Lett.* **105**, 131903 (2014).
- [47] M. Gibertini, F. M. D. Pellegrino, N. Marzari, and M. Polini, *Phys. Rev. B* **90**, 245411 (2014).
- [48] Z. Wu, S. Xu, H. Lu, A. Khamoshi, G.-B. Liu, T. Han, Y. Wu, J. Lin, G. Long, Y. He, Y. Cai, Y. Yao, F. Zhang, and N. Wang, *Nat. Commun.* **7**, 12955 (2016).
- [49] A. B. Bernevig and T. L. Hughes, *Topological Insulators and Topological Superconductors* (Princeton University Press, Princeton, NJ, 2013).
- [50] K. Kaasbjerg, K. S. Thygesen, and K. W. Jacobsen, *Phys. Rev. B* **85**, 115317 (2012).
- [51] B. Ganchev, N. Drummond, I. Aleiner, and V. Fal'ko, *Phys. Rev. Lett.* **114**, 107401 (2015).